

AERODYNAMIC SHAPE OPTIMIZATION OF A WING USING 3D FLOW  
SOLUTIONS WITH SU2 AND RESPONSE SURFACE METHODOLOGY

A THESIS SUBMITTED TO  
THE GRADUATE SCHOOL OF NATURAL AND APPLIED SCIENCES  
OF  
MIDDLE EAST TECHNICAL UNIVERSITY

BY

BERKAY YASİN YILDIRIM

IN PARTIAL FULFILLMENT OF THE REQUIREMENTS  
FOR  
THE DEGREE OF MASTER OF SCIENCE  
IN  
AEROSPACE ENGINEERING

APRIL 2021



Approval of the thesis:

**AERODYNAMIC SHAPE OPTIMIZATION OF A WING USING 3D FLOW SOLUTIONS WITH SU2 AND RESPONSE SURFACE METHODOLOGY**

Submitted by **BERKAY YASİN YILDIRIM** in partial fulfillment of the requirements for the degree of **Master of Science in Aerospace Engineering, Middle East Technical University** by,

Prof. Dr. Halil Kalıpçılar  
Dean, Graduate School of **Natural and Applied Sciences**

Prof. Dr. İsmail Hakkı Tuncer  
Head of the Department, **Aerospace Engineering**

Prof. Dr. İsmail Hakkı Tuncer  
Supervisor, **Aerospace Engineering, METU**

**Examining Committee Members:**

Prof. Dr. Yusuf Özyörük  
Aerospace Eng., METU

Prof. Dr. İsmail Hakkı Tuncer  
Aerospace Eng., METU

Prof. Dr. Serkan Özgen  
Aerospace Eng., METU

Prof. Dr. Ünver Kaynak  
Aerospace Eng., Ankara Yıldırım Beyazıt Uni.

Asst. Prof. Dr. Ali Türker Kutay  
Aerospace Eng., METU

Date: 09.04.2021

**I hereby declare that all information in this document has been obtained and presented in accordance with academic rules and ethical conduct. I also declare that, as required by these rules and conduct, I have fully cited and referenced all material and results that are not original to this work.**

Name, Last name : Berkay Yasin Yıldırım

Signature :

## **ABSTRACT**

### **AERODYNAMIC SHAPE OPTIMIZATION OF A WING USING 3D FLOW SOLUTIONS WITH SU2 AND RESPONSE SURFACE METHODOLOGY**

Yıldırım, Berkay Yasin  
Master of Science, Aerospace Engineering  
Supervisor : Prof. Dr. İsmail Hakkı Tuncer

April 2021, 97 pages

In this study, the aerodynamic shape optimization of a wing is performed by using 3D flow solutions together with response surface methodology. The purpose of this study is to optimize the aerodynamic shape of a wing to achieve the lowest possible drag coefficient while ensuring desired maneuvering capability and lateral stability. Aerodynamic shape optimization is performed for a wing of a turboprop trainer aircraft. Optimization objective and constraints are determined according to mission requirements and the dimensions of turboprop trainer aircraft already operating. Since the objective function and the constraints consist of aerodynamic coefficients, flow solutions are obtained to calculate aerodynamic coefficients by using an open-source RANS solver (SU2). Surrogate models that relate the design parameters to be optimized to the objective function and the constraints are constructed as high-order nonlinear analytical functions with the help of response surface methodology and the design of experiment techniques. In the design of the experiment, a sequential experimentation technique is used. The accuracies of the constructed surrogate models are examined to validate the models. Optimization is performed by using the surrogate models validated and the effect of the different optimization algorithms

(sequential quadratic programming and interior point) and initial conditions on the optimized wing geometry are examined. Optimized wing geometry is compared with the initial geometry in terms of the objective function value and the suitability of the optimized geometry to the constraints is evaluated.

Keywords: Computational Fluid Dynamics, Response Surface Methodology, Design of Experiments, Optimization, Aerodynamic Design

## ÖZ

### **AERODİNAMİK KANAT TASARIMININ SU2 İLE ELDE EDİLEN 3 BOYUTLU AKIŞ ÇÖZÜMLERİ VE CEVAP YÜZEY YÖNTEMİ KULLANILARAK ENİYİLEMESİ**

Yıldırım, Berkay Yasin  
Yüksek Lisans, Havacılık ve Uzay Mühendisliği  
Tez Yöneticisi: Prof. Dr. İsmail Hakkı Tuncer

Nisan 2021, 97 sayfa

Bu çalışmada, 3 boyutlu akış çözümleri ve cevap yüzey yöntemi kullanılarak bir kanadın aerodinamik şeklinin eniyilmesi gerçekleştirilmiştir. Bu çalışmanın amacı, bir kanadın aerodinamik şeklini, elde edilebilecek en düşük sürükleme katsayına, aynı zamanda istenilen manevra kabiliyeti ve yanal kararlılığa sahip olacak şekilde eniyilemektir. Kanat aerodinamik şekil eniyilmesi bir turboprop eğitim uçağı için gerçekleştirilmiş, amaç fonksiyonu ve kısıtlar kullanımında olan turboprop eğitim uçaklarının görev gereklilikleri ve boyutları göz önüne alınarak kararlaştırılmıştır. Amaç fonksiyonu aerodinamik katsayılara bağlı olduğu için 3 boyutlu akış çözümleri, açık kaynaklı Reynolds ortalama Navier-Stokes denklemleri çözücüsü olan SU2 ile elde edilmiştir. Eniyilenecek tasarım parametrelerini amaç fonksiyonu ve kısıtlarla ilişkilendiren vekil modeller cevap yüzey yöntemi ve deney tasarımı teknikleri kullanılarak, yüksek dereceli lineer olmayan analitik fonksiyon formunda oluşturulmuştur. Deney tasarımı sürecinde, sıralı deney tasarımı yöntemi kullanılmıştır. Oluşturulan vekil modellerin hassasiyeti vekil modelleri doğrulamak için incelenmiştir. Eniyileme, doğrulanan vekil model kullanılarak gerçekleştirilmiş olup farklı çözüm algoritmaları (sıralı quadratik programlama ve iç nokta) ve

bařlagıç kořullarının eniyilenen geometriye olan etkileri incelenmiřtir. Eniyilenmiř kanat řekli ve bařlangıç kanat řeklinin amaç fonksiyonu deęerleri karřılařtırılařtırılıp kısıtlara uygunluęu deęerlendirilmiřtir. Eniyilenen geometrinin amaç fonksiyonu deęeri farklı bařlangıç geometrileriyle kıyaslanmıř ve kısıtlara uygunluęu deęerlendirilmiřtir.

Anahtar Kelimeler: Hesaplamalı Akıřkanlar Dinamięi, Cevap Yüzey Yöntemi, Deney Tasarımı, Eniyileme, Aerodinamik Tasarım

To my family...

## ACKNOWLEDGMENTS

I am deeply indebted to Prof. Dr. İsmail Hakkı Tuncer for his relentless support, constructive criticism, sharing his valuable experience, and providing encouragement and patience throughout this study. I also would like to express my deepest appreciation to my committee.

The completion of my dissertation would not have been possible without the support and nurturing of my dear mother and father.

I cannot begin to express my thanks to Hande for always supporting me.

I would like to extend my sincere thanks to Görkem Demir and Mert Cangul for their unwavering support and a great amount of assistance during this study.

I am also grateful to Onurhan Ayhan, Merve Akgünlü, Volkan Mesce, and Eren Duzcu for their practical suggestions and advice.

Thanks should also go to Murat Canıbek, Dr. Erdem Ayan, and Dr. Halil Kaya for believing in my abilities and valuable support.

I very much appreciate my colleagues in flight sciences for providing support and an enjoyable working environment.

Special thanks to Turkish Aerospace for providing the required computational background.

## TABLE OF CONTENTS

ABSTRACT.....	v
ÖZ .....	vii
ACKNOWLEDGMENTS .....	x
TABLE OF CONTENTS.....	xi
LIST OF TABLES .....	xiv
LIST OF FIGURES .....	xv
LIST OF ABBREVIATIONS .....	xviii
LIST OF SYMBOLS .....	xix
CHAPTERS	
1.INTRODUCTION .....	1
1.1 Turboprop Trainers .....	2
1.2 Optimization in Aerodynamic Shape Design.....	5
1.3 Thesis Scope and Outline .....	8
2.DESIGN VARIABLES AND OPTIMIZATION TOOLS .....	11
2.1 Trapezoidal Wing Definition .....	11
2.2 Advantages of Trapezoidal Wing Shape .....	13
2.3 Determination of the Minimum and Maximum Values of the Wing Shape Parameters .....	13
2.4 Determination of the Objective Function .....	15
2.5 Determination of Constraints .....	19
2.6 Optimization Procedure.....	25
2.7 Optimization Algorithms.....	30

3.FLOW SOLUTIONS WITH SU2 .....	33
3.1 Governing Equations .....	33
3.2 Flux Discretization.....	35
3.3 Time Integration .....	35
3.4 Turbulence Model.....	36
3.5 Boundary Conditions .....	36
3.6 Flow Solutions at the Constant Lift Coefficient .....	37
3.7 Grid Generation and Mesh Dependency.....	38
3.8 Flow Solution Scripts.....	42
4.RESPONSE SURFACE METHODOLOGY .....	45
4.1 Full Factorial Designs .....	45
4.2 Determination of Significant Design Parameters .....	46
4.3 Regression Model .....	47
4.4 Validation Process of the Model.....	49
5.RESULTS AND DISCUSSION.....	51
5.1 Two-Level Full Factorial Design.....	51
5.2 Determination of Statistically Significant Parameters.....	54
5.3 Updating the Design of Experiment .....	56
5.4 Validation of Response Surface Models.....	59
5.5 Effect of the Airfoil Profile on the Optimum Solution.....	61
5.6 Optimization of the Wing Planform. ....	69
5.7 Validation of the Optimum Configuration.....	75

6.CONCLUDING REMARKS .....	81
REFERENCES .....	85
APPENDICES	
A.    Additional Design Points for Main Factors.....	93
B.    Additional Design Points for Wingspan – Root Chord Length Interaction	94
C.    Additional Design Points for Tip Chord Length – Root Chord Length	
Interaction .....	95
D.    Additional Design Points for Wingspan – Dihedral Angle Interaction ..	96
E.    Additional Design Points for Root Chord Length – Dihedral Angle	
Interaction .....	97

## LIST OF TABLES

### TABLES

Table 2.1 Design parameters selected to be optimized. ....	12
Table 2.2 Measured wing design parameter values of the competitors. ....	14
Table 2.3 Minimum and maximum values of the design parameters in optimization. .....	15
Table 2.4 The maximum cruise speeds of the competitors [27-30]. ....	16
Table 2.5 Weights of the competitor aircraft.....	17
Table 2.6 Objective function condition. ....	18
Table 2.7 The maneuvering constraint. ....	20
Table 2.8 The lateral stability constraint. ....	23
Table 2.9 The wing reference area constraint .....	23
Table 2.10 The aspect ratio and the taper ratio of competitors. ....	24
Table 2.11 The taper ratio and the aspect ratio constraints. ....	24
Table 4.1 Calculation steps of the Lenth's pseudo standard error. ....	47
Table 5.1 Four levels of the optimization variables. ....	57
Table 5.2 Additional design points to increase wingspan levels to four without including the interactions. ....	57
Table 5.3 Additional design points to include the interaction of wing span and root chord length with four levels. ....	58
Table 5.4 Adjusted $R^2$ values of the regression models. ....	59
Table 5.5 Relative error percentages of regression models.....	60
Table 5.6 Optimum values of the design variables for optimizations with different initial conditions .....	73

## LIST OF FIGURES

### FIGURES

Figure 1.1 Hürkuş turboprop trainer designed and manufactured by Turkish Aerospace [10].	3
Figure 1.2 PC-21 turboprop trainer aircraft designed and manufactured by Pilatus [14].	3
Figure 2.1 Trapezoidal wing parameters.	12
Figure 2.2 Top views of the competitors scaled according to their dimensions. [27-31]	14
Figure 2.3 The lift coefficient ( $C_L$ ) vs the angle of attack.	20
Figure 2.4 The historical trend and the suggested target values of $C_{N\beta}$ [47].	21
Figure 2.5 Military standards MIL-F-8785C [48]	22
Figure 2.6 Optimization process flowchart.	28
Figure 3.1 Boundary conditions and refined grid region.	37
Figure 3.2 Cross-sectional view of the grid.	39
Figure 3.3 Grids generated with a different number of grid points at the root and tip airfoils.	40
Figure 3.4 $C_D$ at 0.528 Mach for different number of grid points on the tip and the root airfoils.	41
Figure 3.5 $C_L$ at 0.528 Mach for different number of grid points on the tip and the root airfoils.	41
Figure 3.6 $C_{R\beta}$ at 0.186 Mach for different number of grid points on the tip and the root airfoils.	42
Figure 5.1 The lift coefficient ( $C_L$ ) value of the geometries in design space.	52
Figure 5.2 The rolling moment change w.r.t. sideslip angle ( $C_{R\beta}$ ) value of the geometries in design space.	53
Figure 5.3 The drag coefficient ( $C_D$ ) at 0.1 lift coefficient ( $C_L$ ) value of the geometries in design space.	53

Figure 5.4 Effect of parameters on the objective function, $C_D$ , where the blue line is drawn at the margin of error. ....	54
Figure 5.5 Effect of parameters on the maneuvering constraint, $C_L$ , where the blue line is drawn at the margin of error. ....	55
Figure 5.6 Effect of parameters on the lateral stability constraint, $C_{RB}$ , where a blue line is drawn at the margin of error. ....	55
Figure 5.7 NACA 63212 and NACA 63415 airfoil profiles. ....	61
Figure 5.8 Comparison of NACA 63212 and NACA 63415 airfoils in terms of lift coefficient ( $C_L$ ). ....	62
Figure 5.9 Comparison of NACA 63212 and NACA 63415 airfoils in terms of drag coefficient ( $C_d$ ). ....	62
Figure 5.10 Comparison of wings with NACA 63212 and NACA 63415 airfoils in terms of lift coefficient ( $C_L$ ). ....	63
Figure 5.11 Comparison of wings with NACA 63212 and NACA 63415 airfoils in terms of drag coefficient ( $C_D$ ). ....	64
Figure 5.12 Design parameter values at each optimization iteration obtained in the first optimization study. ....	66
Figure 5.13 Objective function values at each optimization iteration obtained in the first optimization study. ....	66
Figure 5.14 Design parameter values at each optimization iteration obtained in the second optimization study. ....	67
Figure 5.15 Objective function values at each optimization iteration obtained in the second optimization study. ....	68
Figure 5.16 The lift coefficient value at each optimization iteration obtained in the second optimization study. ....	68
Figure 5.17 The objective function value during optimization steps. ....	70
Figure 5.18 Objective function value ( $C_D$ at 0.528 Mach 0.1 $C_L$ ) at each optimization iteration. ....	71
Figure 5.19 Maneuvering constraint value ( $C_L$ at 0.4 Mach) at each optimization iteration. ....	71

Figure 5.20 Lateral stability constraint value ( $C_{RB}$ at 0.4 Mach) at each optimization iteration. ....	72
Figure 5.21 Wing configurations at different optimization steps. ....	74
Figure 5.22 The optimum wing geometry from different views. ....	74
Figure 5.23 The drag polar at $M^\infty = 0.528$ for the initial and the optimum wings. ....	75
Figure 5.24 The surface pressure coefficient distributions for initial and optimum wings at $M^\infty = 0.528$ from the top view. ....	76
Figure 5.25 The lift coefficient ( $C_L$ ) vs angle of attack at $M^\infty = 0.4$ . ....	76
Figure 5.26 The rolling moment coefficient ( $C_R$ ) at different sideslip angles at $M^\infty = 0.186$ .....	77
Figure 5.27 The pitching moment coefficient change vs the lift coefficient for the initial and the optimum wings.....	77
Figure 5.28 The initial and the optimum wings. ....	78
Figure 5.29 The optimized wing attached to the turboprop trainer aircraft EMB 312 body.....	79

## LIST OF ABBREVIATIONS

### ABBREVIATIONS

AoA	Angle of Attack
AoS	Angle of Sideslip
AUSM	Advection Upstream Splitting Method
BFGS	Broyden-Fletcher_Goldfarb-Shanno
CFD	Computational Fluid Dynamics
DC	Drag Count, Drag Coefficient Multiplied by $10^4$
FVM	Finite Volume Method
HLLC	Harten-Lax-van Leer-Contact
JST	Jameson-Schmidt-Turkel
KEAS	Knots Equivalent Airspeed
KKT	Karush-Kuhn-Tucker
KTAS	Knots True Airspeed
PSE	Pseudo Standard Error
RANS	Reynolds-averaged Navier-Stokes
RSM	Response Surface Methodology
SQP	Sequential Quadratic Programming
SU2	Stanford University Unstructured

## LIST OF SYMBOLS

### SYMBOLS

$C_l$	Lift Coefficient of an Airfoil
$C_d$	Drag Coefficient of an Airfoil
$C_L$	Lift Coefficient of a Wing
$C_D$	Drag Coefficient of a Wing
$C_R$	Rolling Moment Coefficient of a Wing
$C_{R\beta}$	Rolling Moment Coefficient Derivative w.r.t Sideslip Angle of a Wing
$C_{N\beta}$	Yawing Moment Coefficient Derivative w.r.t Sideslip Angle of a Wing
$V_H$	The Maximum Cruise Speed
$\rho$	Density of a fluid
$R^2$	Coefficient of Determination
$\bar{v}$	Velocity of a Fluid
$p$	Static Pressure
$\bar{I}$	Identity Matrix
$\bar{\tau}$	Stress Tensor
$\mu$	Viscosity
$\Delta S_{ij}$	Area of the Cell Face
$\kappa$	Thermal Conductivity
$ \Omega_i $	Volume of the Control Volume
$R_i(U)$	Residual Term
$\bar{F}^c$	Convective Flux Vector
$\bar{F}^v$	Viscous Flux Vector
$y^+$	Nondimensional Distance
$\delta$	Boundary Layer Thickness
$Re$	Reynolds Number
$T$	Static Temperature

$\varepsilon$	Error of the Model
$\beta$	Regression Coefficients
$y$	Response Value
$\mathbf{X}$	Model Matrix
$\mathbf{b}$	Solution Vector of Regression Coefficients
$\mathbf{y}$	Response Vector
$M_\infty$	Freestream Mach Number

## CHAPTER 1

### INTRODUCTION

The wing provides the majority of the lift an airplane requires for flight [1]. Besides, drag due to lift which is the drag generated by lift force due to pressure difference is mainly generated by wings that affect the drag polar of the aircraft. Moreover, the maximum lift coefficient, the lift coefficient at a certain angle of attack and sideslip angle condition, and the lift coefficient change with respect to the angle of attack and sideslip angle mainly depend on the aerodynamic shape of the wing. Furthermore, the wetted area of the wing affects parasite drag as well. Therefore, the aerodynamic shape significantly affects the aerodynamic coefficients mentioned which influence the aircraft performance at different flight conditions. Some of the performance parameters and affecting aerodynamic forces and coefficients that mainly depend on the aerodynamic shape of the wing are explained as follows;

- The range and endurance of the aircraft depend on the lift to drag ratio [2].
- Stalling speed is the speed that an aircraft could be flown at least in an equilibrium where the thrust is equal to the drag and stalling speed depends on the maximum lift coefficient [2].
- The absolute ceiling of the aircraft is a function of lift coefficient change with respect to the angle of attack [3].
- Take-off and landing distances depend on the lift to drag ratio [3].
- The maximum cruise speed mainly depends on parasite drag and the flight envelope also depends on the maximum lift coefficient [3].
- The drag of the aircraft plays an important role in the rate of climb as well [4].

- The lift coefficient change with respect to the angle of attack has a significant effect on the roll rate of an aircraft which is important for maneuverable aircrafts such as fighters [5].

Therefore, the aerodynamic shape of the wing is critical for aircraft flight performance at different flight phases. In addition to the effects of the aerodynamic shape of the wing on aircraft performance, it has also a crucial effect on the aircraft stability and the flying quality that is the aircraft characteristic related to ease and precision of usage while the pilot is performing a mission.

Considering the longitudinal stability, lift, lift change with respect to the angle of attack, location of the aerodynamic center, and wing downwash have an important effect and depend on the aerodynamic shape [7].

In terms of lateral stability, the dihedral angle which is one of the wing shape parameters has the most significant influence because it directly affects the rolling moment coefficient change with respect to sideslip angle [8]. Also, the location of the aerodynamic center of the wing affects lateral stability as well [9].

Finally, the drag generated by wings has an important effect on the directional stability because the drag difference between the wings generates a yawing moment under the sideslip. Consequently, as it is explained, the aerodynamic shape of the wing is important for the aircraft performance and flying qualities.

## **1.1 Turboprop Trainers**

Turboprop trainer aircraft are used in military pilot training. Turboprop trainer aircraft are mainly powered with a single turboprop engine and consist of two seats for a student pilot and a training officer. There are various turboprop trainer aircrafts available in the market and still operating, designed, and produced in different years. As an example of a turboprop trainer, the Hürkuş aircraft that is designed and manufactured by Turkish Aerospace is shown in Figure 1.1. Another example of a

turboprop trainer, the PC-21 aircraft that is designed and manufactured by Pilatus is shown in and Figure 1.2.



Figure 1.1 Hürkuş turboprop trainer designed and manufactured by Turkish Aerospace [10].



Figure 1.2 PC-21 turboprop trainer aircraft designed and manufactured by Pilatus [14].

Day by day, the flight instrumentation capability and the flying quality of turboprop trainer aircraft have increased. Therefore, various turboprop trainer aircraft in operation offer different training capabilities which change the usage of the aircraft

during the military pilot training. According to the capability of the turboprop trainer aircraft, the training concept changes which changes the flight hour of the student with a turboprop trainer aircraft. In addition, different air forces follow different training procedures and flight hours for military pilots with turboprop trainer aircraft.

As an example, the Turkish Air Force uses KT-1T, a turboprop trainer aircraft, in basic training for a jet flight to give student pilots the ability of handling a jet trainer aircraft [11]. Another example is that the United States Air Forces (USAF) uses T-6 Texan II, a turboprop trainer aircraft, in the Euro-NATO Joint Jet Pilot Training program. T-6 Texan II is used for mastering contact, instrument, low-level, and formation flying to prepare student pilots for a jet trainer [12]. Swiss Air Force has started using PC-21, a turboprop trainer aircraft, for instrument flight, formation flying, navigation, air-to-ground attack, air policing, and air warfare training [13]. After training is completed with PC-21, student pilots directly start to fly with Boeing F/A-18, a fighter aircraft, without flying with a jet trainer aircraft [13].

Even various training programs are applied by different air forces, turboprop trainer aircraft are used for most of the military pilot training programs. In general, they are used to train student pilots the basics of flight and give student pilots the ability of handling a jet trainer. Therefore, it is expected from turboprop trainer aircraft to have maneuverability and a large flight envelope compared to general aviation aircraft in order to train student pilots to be able to handle jet trainer aircraft. Besides, turboprop trainer aircraft should have flight instrumentation that have similar usage with instrumentation of a fighter aircraft in order to train student pilots for instrumented flights.

Instead of the traditional usage of turboprop trainer aircraft, there is a demand to expand the flight envelope and maneuverability capability of turboprop trainer aircraft lately. The main reason behind this demand is to use turboprop trainer aircraft for some of the training performed with jet trainer aircraft in the traditional approach. By increasing the training hours of a student pilot with turboprop trainer aircraft and

decreasing training hours of the student pilot with jet trainer aircraft, the cost of training the pilot decreases.

To achieve this aim, turboprop trainer aircraft should fly at some of the flight regimes where jet trainer aircraft could fly and it should be as highly maneuverable as a jet trainer. It may not be possible to perform flight with a turboprop trainer aircraft in the entire flight envelope of a jet trainer aircraft. However, compared to traditional turboprop trainer aircraft, it is possible that some of the training performed with jet trainer aircraft could be replaced by training performed with turboprop trainer aircraft by expanding the flight envelope and maneuverability of the turboprop trainer aircraft. With the flying and maneuvering capability of PC-21, Pilatus offers the training concept that replaces jet trainer aircraft with turboprop trainer aircraft and classifies PC-21 as a next-generation trainer [15]. However, expanding the flight envelope and increasing the maneuverability of the traditional turboprop trainer aircraft is a challenging problem. Therefore, optimization techniques become important in the design of turboprop trainer aircraft.

## **1.2 Optimization in Aerodynamic Shape Design**

As explained, the aerodynamic shape of the wing is important for the performance and flying qualities of an aircraft. Therefore, optimization techniques could be used to design the aerodynamic shape of a wing to satisfy different performance requirements of various aircraft to achieve the optimum design.

As an example, the range and endurance of an aircraft is a function of lift to drag ratio which mainly depends on the aerodynamic shape of the wing and significant for commercial aircraft [16]. Without losing the required lift coefficient, decreasing the drag coefficient can be achieved with the aerodynamic shape optimization of a wing which is important for turboprop trainer aircraft to have a large flight envelope. Another example is that it is important to have a lower turn radius for fighters which is a function of the lift coefficient [17]. Therefore, optimization could be performed

to design the aerodynamic shape of a wing that is the main source of the lift to decrease turn radius for a fighter which is important during combat. Consequently, aerodynamic shape optimization of a wing could be performed for various types of aircraft to achieve different goals. There are different approaches in the literature for the aerodynamic shape optimization of a wing.

The optimization process of a wing includes the calculation of aerodynamic coefficients which are used in objective functions and constraints. Even though there are different methods to calculate aerodynamic coefficients such as panel and vortex lattice methods, due to the increase in the computational power in the last decades, Reynolds-averaged Navier-Stokes (RANS) solutions became more popular lately to achieve higher accuracy.

Different optimization techniques could be used to optimize the aerodynamic shape of a wing using RANS solutions. In the literature, optimization algorithms used to optimize the aerodynamic shape of a wing are based on mainly two different approaches that are gradient-based or gradient-free (i.e., derivative-free).

Gradient-based optimization algorithms require the calculation of the gradient of the objective function. In the aerodynamic shape optimization, when RANS equations are solved to obtain aerodynamic coefficients used in the objective function, the gradient of the objective function could not be calculated analytically. Therefore, numerical approximations of the gradient could be obtained or surrogate models could be used to replace RANS equations with analytical functions. Numerical approximation of the gradient could be obtained by using finite difference or adjoint methods. The finite difference method requires a calculation of the objective function at different values of the independent variables to calculate the gradient. However, the adjoint method requires a solution of the adjoint matrix to calculate the gradient of the function. If a surrogate model is constructed to replace RANS solutions, the gradient vector could be calculated from the model analytically. However, in derivative-free approaches calculation of the gradient is not required. The advantages

and disadvantages of the approaches for the aerodynamic shape optimization of a wing are discussed in Chapter 2.

Examples of aerodynamic shape optimization using gradient-based and gradient-free optimization algorithms are available in the literature. As an example, Peiging and Epstein performed an aerodynamic shape optimization by using RANS solutions and the genetic algorithm which is a gradient-free method to achieve the lowest possible drag coefficient at a constant lift coefficient by providing desired pitching moment coefficient and wing area in a transonic regime for Onera M6 wing [18]. Bezier curves are used to parametrize airfoils and linear interpolation is performed between the root and the tip airfoil sections. As a result, a reduction in the drag coefficient while providing the desired lift and moment coefficients is achieved by weakening the shock.

Another study is performed by Dumont and Méheut which is a gradient-based aerodynamic shape optimization of a common research model (CRM) wing alone and wing-body-tail configurations by using RANS solutions [19]. Adjoint solutions are obtained for gradient calculations required in the optimization [19]. The freeform grid deformation method is used for grid deformation and the modified method of feasible directions (MMFD) method is used for line search. As a result, a higher lift to drag ratio is achieved, the drag coefficient is decreased, and trim conditions are not changed by providing the required lift and moment coefficients.

The study performed by Wang, Han, Song, Wang, and Wu could be given as an example of using surrogate models to replace RANS solutions for the aerodynamic shape optimization [20]. Common research model with wing, body, and tail is optimized by using surrogate models. Surrogate models are constructed with different methods that are kriging, polynomial response surface, radial-basis functions, and artificial neural networks. The design of experiment technique is used to determine sample points for the construction of a surrogate model. As a result, lower drag coefficient values are achieved without changing the lift coefficient

considering trim drag. Consequently, different approaches and different methodologies could be used to optimize the aerodynamic shape of a wing.

### **1.3 Thesis Scope and Outline**

Various types of aircraft should satisfy different performance requirements and the desired flying quality related to the mission profile of the aircraft. Various aerodynamic shapes of the aircraft have a significant effect on different performance parameters and flying quality. Besides, the aerodynamic shape optimization could be performed to design the aerodynamic shape of a surface to satisfy requirements related to aircraft performance and flying quality using different optimization algorithms explained in Section 1.2.

In this study, it is aimed to perform an aerodynamic shape optimization of an aerodynamic surface by using RANS solutions and surrogate models. Due to the importance of the aerodynamic shape of a wing as explained, the aerodynamic shape optimization is performed for a wing. Trapezoidal wing shape is used to be optimized and parameters that define the aerodynamic shape of a trapezoidal wing are explained in Chapter 2. The airfoil profiles are not included in the optimization, but the effect of the airfoil profile on the optimum geometry is examined and results are presented in Chapter 5.

To perform the aerodynamic shape optimization, reasonable objective functions and constraints should be assigned. To assign reasonable objective functions and constraints, the mission profile of the aircraft should be known. As it is explained in Section 1.1, the design of a turboprop trainer aircraft is highly challenging and is considered as an optimization problem. In this study, the aerodynamic shape optimization of a wing for a turboprop trainer aircraft is performed. However, it should be noted that the methodology used in this study is applicable for any aerodynamic surface of any aircraft type.

To assign reasonable objective functions and constraints, the mission profile of the turboprop trainer aircraft is considered. To increase the flight envelope of the turboprop trainer aircraft due to reasons explained in Section 1.1, aerodynamic shape optimization of a wing is performed to decrease the drag coefficient [21]. While minimizing the drag coefficient, the lift coefficient should not decrease to satisfy the required lift coefficient for the cruise. Therefore, the lift coefficient is constrained while minimizing the drag coefficient.

Even if the lift coefficient is constrained at the cruise condition where the drag coefficient is minimized, the lift coefficient is also constrained in the maneuvering condition to satisfy a desired maneuvering capability. In addition to the maneuvering capability, the lateral stability of the aircraft is also constrained because the dihedral angle which is one of the parameters that defines the aerodynamic shape of the wing has a significant effect on lateral stability [21].

Also considering the wing weight, the aspect ratio and the taper ratio of the wing are constrained as well. In addition, since the wing loading has an important effect on the mission profile, the wing area is constrained. Flow conditions for the objective function and constraints and values of the constraints are determined according to mission requirements and dimensions of turboprop trainer aircraft already operating explained in Chapter 2 in detail.

Since the objective function and some of the constraints are functions of aerodynamic coefficients, RANS solutions are obtained to calculate aerodynamic coefficients. An open-source RANS solver SU2 is used to calculate aerodynamic coefficients. Details of the RANS solution methods, boundary conditions, and grids used in this study are explained in Chapter 3 in detail.

In this study, the surrogate model based optimization approach explained briefly in Section 1.2 is used. In this approach, surrogate models are constructed to calculate aerodynamic coefficients required in the objective function and constraints based on RANS solutions. High-order nonlinear functions are used as surrogate models to calculate required aerodynamic coefficients using response surface methodology.

Constructed surrogate models are validated by comparing results of analytical functions with the RANS solutions at the randomly selected design points. With this surrogate model based approach, it is aimed to construct an optimization setup that is flexible for trade-off studies. Details of the surrogate model construction are explained in Chapter 4.

The boundaries of the design space and the design points used to construct surrogate models should be reasonable to construct surrogate models that have high accuracy. Dimensions of turboprop trainer aircraft already operating are used to determine the boundaries of the design space. In this study, the sequential experimentation method, a design of experiment method, is used to determine design points used to construct surrogate models. In this approach, instead of using full factorial designs, significant interaction terms are determined with statistical approaches and design points in the full factorial design that are related to statistically insignificant terms are eliminated. It is aimed to decrease the number of design points that require RANS solutions compared to the traditional full factorial designs by using the sequential experimentation approach. Details of the design of experiment methodology are explained in Chapter 4.

After constructing and validating surrogate models, optimization is performed by using analytical functions. Since functions are high-order nonlinear functions, nonlinearly constrained optimization algorithms are used in this study. Details of the optimization algorithms and optimization flowchart are explained in Chapter 2.

Optimization is performed by starting from different initial conditions to observe the effect of the initial condition on the optimization. In addition, different optimization algorithms, sequential quadratic programming and interior point, are used to examine the effect of the optimization algorithm on the optimization. Since surrogate models include model errors, RANS solutions are obtained for the optimum configuration and initial configuration to validate the optimum configuration. All results related to the topics explained are presented and discussed in Chapter 5 in detail.

## CHAPTER 2

### DESIGN VARIABLES AND OPTIMIZATION TOOLS

In this chapter, the methodology to determine parameters used in the optimization that define the aerodynamic shape of the wing is explained first. The boundaries of the design space are then presented that are determined according to mission requirements and the dimensions of turboprop trainer aircraft already operating. Details of the optimization process are also clarified by showing the optimization process flowchart. Finally, the determination of the objective function, constraints, and algorithms used in the optimization are discussed in detail in this chapter.

#### 2.1 Trapezoidal Wing Definition

Trapezoidal wing shape is a basic wing shape used in the traditional design approach [22]. The wings that have straight edges at the root and tip, straight lines at the leading and trailing edges, and a tapered planform with or without sweep are defined as trapezoidal wings. In addition, the trapezoidal wing planform is the most common planform shape in use for many aircraft designs such as Dassault Rafale, F-35, Mig-35, and also turboprop trainers [23,24]. Trapezoidal wings might have a sweep, dihedral, and tip twist which are included in this study as shape parameters to define the wing shape. Parameters that define the trapezoidal wing shape are shown in Figure 2.1. In addition to the parameters defined in Figure 2.1, airfoil profiles also define the aerodynamic shape of the wing.

It should be noted that, instead of the leading edge or trailing edge sweep angles, quarter chord sweep angle is used in this study because it is commonly used in the scientific literature such as reference figures of U.S.A.F Datcom [25,26].

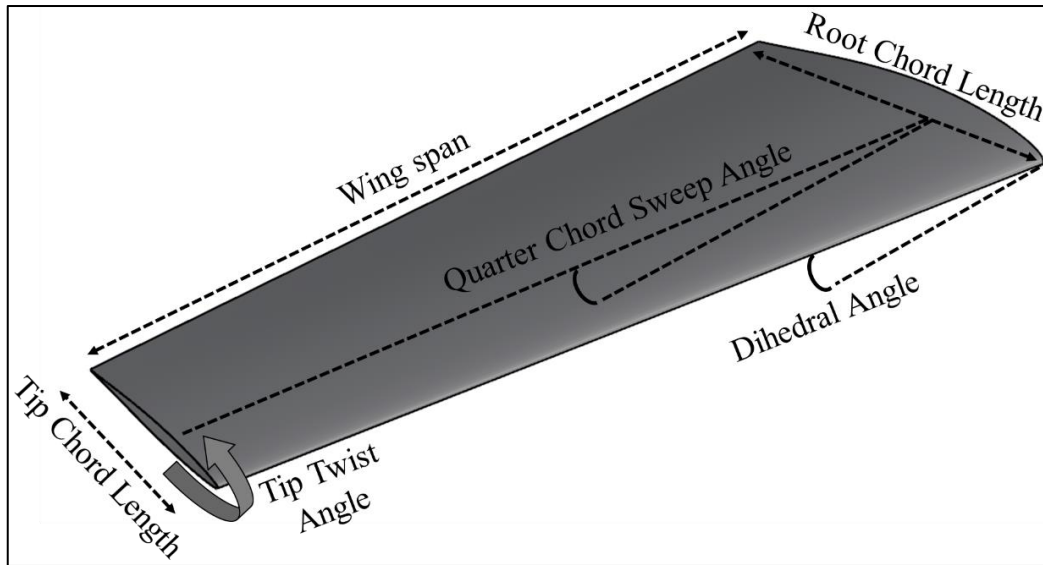


Figure 2.1 Trapezoidal wing parameters.

As a result, the aerodynamic shape of the wing is defined with eight parameters that are wing root and tip chord lengths, wingspan, quarter chord sweep, dihedral and tip twist angles, and wing root and tip airfoil profiles according to the trapezoidal wing approach.

In this study, the airfoil profile is not included among the optimization parameters. However, the effect of airfoil profiles on the optimum geometry is studied by performing optimization for two different airfoils presented in Chapter 5. Wing shape parameters (i.e., optimization variables) that will be optimized in this study are given in Table 2.1.

Table 2.1 Design parameters selected to be optimized.

<b>Parameters</b>
Root Chord Length
Tip Chord Length
Wingspan
Dihedral Angle
Quarter Chord Sweep Angle
Tip Twist Angle

## **2.2 Advantages of Trapezoidal Wing Shape**

Defining the aerodynamic shape of the wing geometry as a trapezoidal shape has many advantages even though it is the simplest geometric shape for a wing. The main advantage of the trapezoidal wing approach is that it requires basic mathematics to describe the wing shape. With the help of mathematical simplicity, it is much easier to generate scripts for the automated geometry generation process used in RANS solutions.

In addition, most of the designed aircraft use trapezoidal wings and a lot of historical and experimental data are available which could be used while designing the aerodynamic shape of the wing.

## **2.3 Determination of the Minimum and Maximum Values of the Wing Shape Parameters**

It is important to determine a possible and reasonable minimum and maximum values of the design parameters during the optimization process to achieve an optimum design. In the optimization process, the optimum will be searched among the minimum and maximum values of the aerodynamic shape parameters (i.e., boundaries of the design space). Since surrogate models will be used in the optimization that is constructed among the boundaries of the design space, surrogate model accuracy is affected by the boundaries of the design space. Having a large design space might decrease the accuracy of the surrogate model or increase the number of RANS solutions to increase accuracy. However, defining a small design space might result in missing a better optimum design. Therefore, the minimum and maximum values of the design parameters should be determined with a reasonable approach.

In this study, wing geometries of the competitor aircraft are examined to assign reasonable minimum and maximum design parameter values. Pilatus PC-21, KAI KT-1 Woongbi, Embraer EMB 314 Super Tucano, and TAI Hurkus aircraft are

selected as competitors to measure wing design parameter values. Top views of the aircraft are obtained and scaled according to their dimensions with the help of the Rhinoceros computer-aided design (CAD) tool [27-32]. Top views of the competitors scaled according to their dimensions are shown in Figure 2.2.

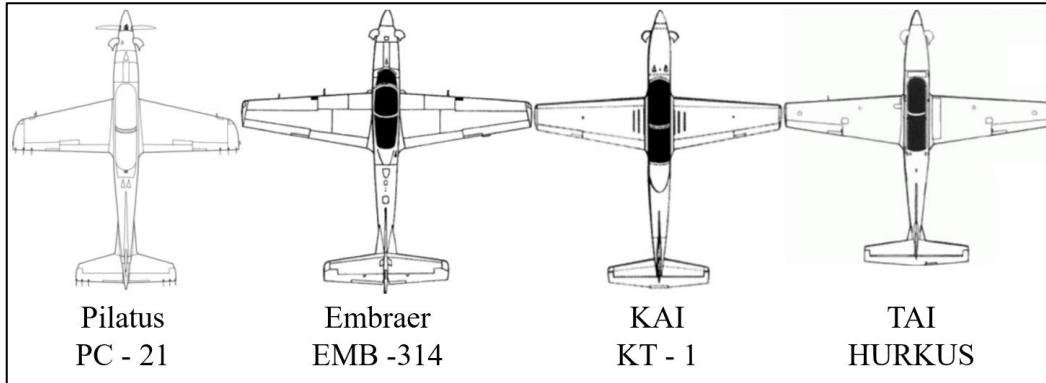


Figure 2.2 Top views of the competitors scaled according to their dimensions. [27-31]

Measured design parameters from the scaled views with the help of the CAD tool of the competitors are shown in Table 2.2 [32].

Table 2.2 Measured wing design parameter values of the competitors.

<b>Parameter</b>	<b>KAI KT-1 Woongbi</b>	<b>Pilatus PC-21</b>	<b>Embraer EMB 314 Super Tucano</b>	<b>TAI Hurkus</b>
Wing Span (m)	10.486	8.200	11.146	9.960
Root Chord Length (m)	2.061	2.286	2.334	2.220
Root Tip Length (m)	0.954	1.244	1.006	0.976
Taper Ratio	0.463	0.544	0.431	0.440
Aspect Ratio	6.956	4.646	6.674	6.233
Wing Area (m <sup>2</sup> )	15.808	14.473	18.614	15.916
Quarter Chord Sweep Angle (degrees)	0	9	0	0

It is expected to obtain an optimum design among the design parameters of the competitors. However, to search optimum by including design parameter values outside of the competitor values, the minimum and maximum values are determined to be 10% higher and lower than the maximum and minimum of the competitors respectively. It should be noted that 10% is the approximate ratio of the maximum difference between the wing areas and the mean of the wing areas.

The wing twist angle rarely exceeds  $3^\circ$  in a counterclockwise direction which is assumed as a negative in this study [23]. Hence, the minimum of the wing twist is selected as  $-3^\circ$  and the maximum is selected as  $0^\circ$  which is the case without any tip twist.

Similarly for the dihedral angle, historical trend does not exceed  $10^\circ$  which is selected as the maximum value and  $0^\circ$  is selected as the minimum value which is the case without dihedral. As a result, the minimum and maximum values of the design parameters (i.e., boundaries of the design space) are determined and given in Table 2.3.

Table 2.3 Minimum and maximum values of the design parameters in optimization.

	Wing Span (m)	Root Chord Length (m)	Tip Chord Length (m)	Dihedral Angle (degrees)	Quarter Chord Sweep Angle (degrees)	Tip Twist Angle (degrees)
Minimum	7.38	1.85	0.86	0	0	0
Maximum	12.26	2.57	1.37	10	10	-3

#### 2.4 Determination of the Objective Function

The objective function is the function that defines the goal of an optimization process. As it is explained in Chapter 1, having a large flight envelope is desired in turboprop trainers to train student pilots by flying at higher speed regimes. The maximum cruise speed ( $V_H$ ) of an aircraft is important to determine the flight

envelope borders of an aircraft [41]. The maximum cruise speed of an aircraft depends on the thrust available and the drag coefficient [42]. To achieve the highest possible speed, a minimum drag is required for an aircraft. Since the wing area is constrained due to considerations explained in Section 2.5, instead of the drag, the drag coefficient is used in the objective function in this study. After all, the goal of this study is to optimize a turboprop trainer wing to achieve the drag coefficient as low as possible.

To determine the flow condition where the objective function is evaluated, competitor values are used. The maximum cruise speed and the corresponding atmospheric conditions of competitor aircraft are shown in Table 2.4.

Table 2.4 The maximum cruise speeds of the competitors [27-30].

<b>Parameter</b>	<b>KAI KT-1 Woongbi</b>	<b>Pilatus PC-21</b>	<b>Embraer EMB 314 Super Tucano</b>	<b>TAI Hurkus</b>
Maximum Cruise Speed	280	337	280	310
( $V_H$ )	KTAS	KTAS	KTAS	KTAS
Corresponding Altitude (feet)	14993	10000	0	0
Sea Level Maximum Mach Number	0.447	0.528	0.423	0.469

Calculation of the maximum cruise speed for an aircraft is an iterative process and all components of the aircraft play an important role due to the generation of the drag and the lift. In addition to aerodynamic coefficients, available thrust has also an effect on the maximum cruise speed [43]. Therefore, as an assumption, the maximum Mach number condition among the competitors is selected as a Mach number of the

flow where the objective function, the drag coefficient, is evaluated. This assumption is a similar approach with assigning the target maximum cruise Mach number in a design process.

According to Table 2.4, the maximum Mach number corresponds to 0.528 Mach which will be the Mach number where the drag coefficient is evaluated. Therefore, 0.528 Mach number at sea level condition is determined as the flow condition where the objective function, the drag coefficient, is evaluated.

Ideally, the maximum cruise speed is achieved where the lift coefficient is equal to zero because the minimum drag coefficient is achieved. However, it is not possible in reality because an aircraft has a weight. Aircraft should be able to cruise by sustaining the required lift coefficient at maximum speed to balance the weight. Since changing design parameters also affect the lift coefficient of the wing, it is possible to optimize a wing that results in the minimum drag coefficient but cannot sustain the required lift coefficient at the maximum cruise speed condition. Therefore, in this study, the drag coefficient is minimized at 0.528 Mach and the lift coefficient is kept constant.

To determine the value of the lift coefficient kept constant, the weight of the aircraft that wing is optimized for and the reference area of the wing should be known. The average values of the competitors given in Table 2.5 are used to calculate the required lift coefficient.

Table 2.5 Weights of the competitor aircraft.

<b>Parameter</b>	<b>KAI KT-1 Woongbi</b>	<b>Pilatus PC-21</b>	<b>Embraer EMB 314 Super Tucano</b>	<b>TAI Hurkus</b>
Weight (kg)	2540	3100	3900	3650

According to Table 2.5, the average weight of the competitors is 3298 kg which is the assumed weight of the aircraft that the wing is optimized for. For the reference area, an average value of the wing loadings of the competitors and the ratio of the weight to the wing area, are used that are obtained from Table 2.2 and Table 2.5. As a result, the reference area is calculated as 16.21 m<sup>2</sup>. For a freestream velocity of 0.528 Mach which is equal to 180 m/s at sea level, the required lift coefficient ( $C_L$ ) is calculated as 0.1 by solving Equation (1) for  $C_L$  [43].

$$C_L = \frac{W}{q_\infty S_{ref}} \quad (1)$$

In Equation (1),  $q_\infty$  is the dynamic pressure,  $S_{ref}$  is the reference wing area, and  $W$  is the weight of the aircraft. As a result, the objective function is determined and defined in Table 2.6.

Table 2.6 Objective function condition.

<b>Objective Function</b>	<b>Mach</b>	<b>Altitude</b>	<b>Lift Coefficient</b>
Minimize $C_D$	0.528	Sea Level	0.1

For each design point, the angle of attack corresponding to 0.1 lift coefficient changes as the shape parameters change, which will require additional RANS solutions to be performed at various angles of attack in the traditional approach. However, it is possible to perform fixed lift coefficient RANS simulations with the help of open-source software SU2. In this study, the fixed lift coefficient RANS solutions are obtained using SU2 and the angle of attack of the flow condition where the objective function is evaluated changed by SU2 to satisfy the fixed lift coefficient. Details of the fixed lift coefficient calculations are explained in Chapter 3.

## 2.5 Determination of Constraints

The drag could be separated into components called the parasite drag (i.e., the zero-lift drag) and the induced drag (i.e., the lift-dependent drag) [44]. Hence, decreasing the drag coefficient might result in a decrease in the lift coefficient due to induced effects. Even though the lift coefficient is constrained to be constant to sustain the required lift coefficient for the cruise condition, it should also be constrained considering the maneuvering capability of the aircraft. Therefore, the lift coefficient is also constrained at a different flight condition.

For this purpose, the loop maneuver on which the balance between the lift and the drag coefficient of the aircraft plays an important role is considered. It is required to enter a loop maneuver where the aircraft should generate the required lift coefficient to sustain the desired pull-up.

During the design phase of an aircraft, requirements are already determined according to maneuvers. However, for this study, the constraint condition is assumed according to the maneuvering condition of another aircraft. According to the F-16 multi command handbook, it is suggested to perform a loop maneuver with 4g pull-up at 10000 feet altitude [45]. For the maneuvering speed, competitor PC-21 value is used which is 220 KEAS corresponds to 0.4 Mach at 10000 feet altitude [46].

After determining the altitude, the pull up g, and the speed, the required lift coefficient is calculated using Equation (1) by assigning the weight as four times 3298 kg and solving the equation for the lift coefficient ( $C_L$ ). As a result, the lift coefficient required is calculated as 1.05 to sustain 4g pull-up by solving Equation (1) for  $C_L$ .

It is not possible to fix the lift coefficient as previously done in the objective function condition because the lift coefficient is the response of the constraint. Therefore, the angle of attack should be fixed to a reasonable value for the constraint condition. It is important to assign a reasonable angle of attack for the constraint because otherwise, the optimum design might not exist to satisfy the desired constraint.

To determine the angle of attack, a RANS solution is obtained for the wing that has average values of the design parameters which corresponds to the middle point of the design space at 0.4 Mach 10000 feet altitude condition. The lift coefficient vs the angle of attack is shown in Figure 2.3.

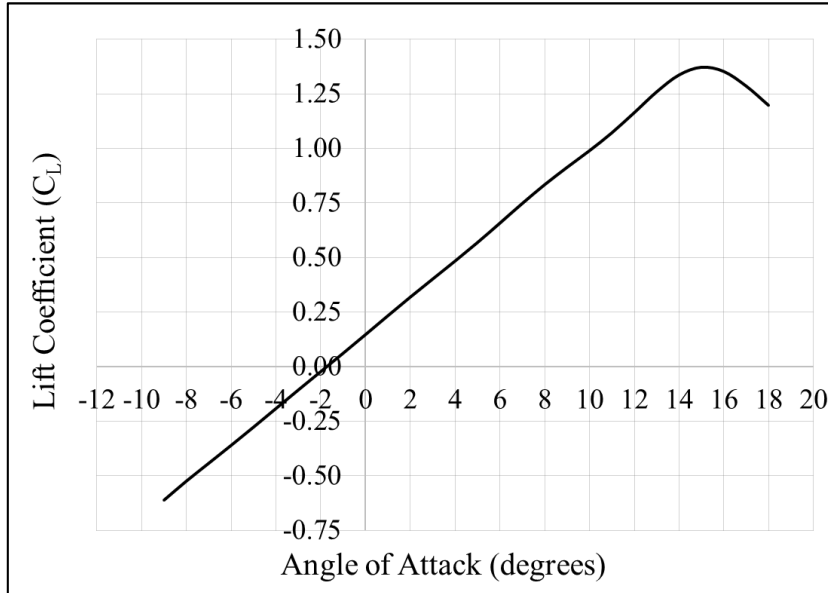


Figure 2.3 The lift coefficient ( $C_L$ ) vs the angle of attack.

It is observed in Figure 2.3 that a value of 1.05  $C_L$  is achieved approximately at 10° of the angle of attack which is assigned as the angle of attack where the maneuvering constraint is set as shown in Table 2.7.

Table 2.7 The maneuvering constraint.

<b>Constraint</b>	<b>Speed</b>	<b>Altitude</b>	<b>Mach</b>	<b>Angle of Attack</b>
$C_L \geq 1.05$	220 KEAS	10000 feet	0.4	10°

In addition to the maneuvering constraint, since the dihedral angle is a design parameter which is one of the most important parameters that affects lateral stability of the aircraft, a lateral stability constraint is also defined [8]. The change in the

rolling moment coefficient with respect to sideslip angle ( $C_{RB}$ ) is an important parameter in the lateral stability of an aircraft which is also constrained in this study.

To assign reasonable values to  $C_{RB}$ , the historical data is used. According to the historical data,  $C_{RB}$  should be of a negative sign with a magnitude about half that of the  $C_{NB}$  value at subsonic speeds [47]. The historical data and the suggested target values of the  $C_{NB}$  are given in Figure 2.4. For the desired level of lateral stability, at least the suggested target value should be satisfied [47].

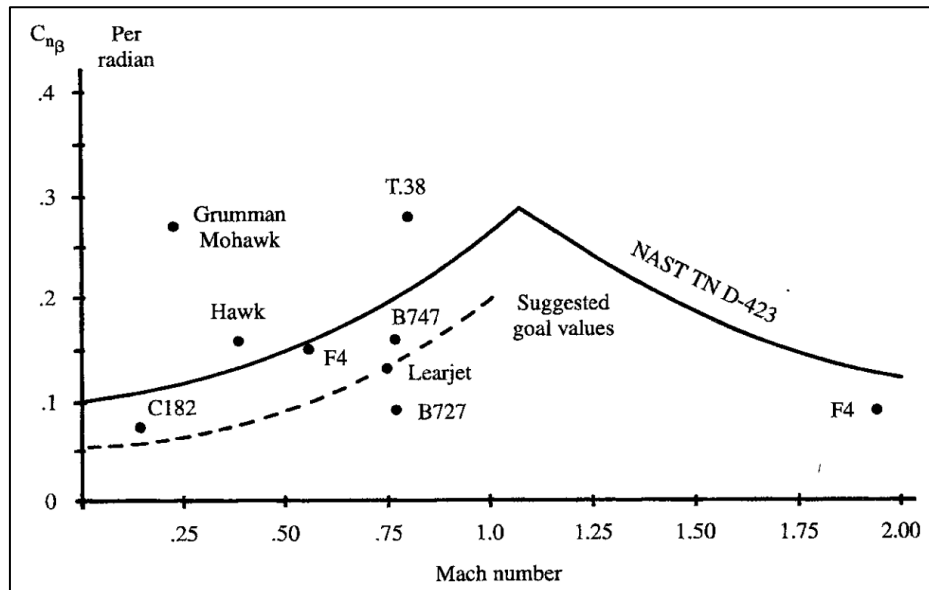


Figure 2.4 The historical trend and the suggested target values of  $C_{NB}$  [47].

To determine the target value from Figure 2.4, the Mach number condition where the stability constraint is evaluated should be determined. For this purpose, approach speed is used to simulate the touch-and-go condition.

The approach speed should be considered as 1.3 times the stall speed [22]. The stall speed calculated using Equation (1) by substituting the maximum lift coefficient ( $C_{Lmax}$ ) and solving the equation for the velocity. The maximum lift coefficient value of the wing that is the middle point of the design space is used to assign a reasonable stall speed that will cover all the design space approximately as given in Figure 2.3. By substituting 1.37 as the maximum lift coefficient at sea level, the stall speed is calculated as 0.143 Mach.

After calculating the stall speed, the approach speed is calculated as 0.186 Mach. For the wing at the middle point of the design space at 0.186 Mach sea level condition, by solving Equation (1) for  $C_L$ , the required  $C_L$  corresponding to the weight is calculated. The angle of attack corresponding to the calculated  $C_L$  is obtained as  $8^\circ$  (Figure 2.3).

For 0.186 Mach speed, from Figure 2.4, the suggested target value of the  $C_{NB}$  is approximately 0.05 per radians and  $C_{RB}$  is -0.025 per radians that equals -0.0004363 per degree. Since  $C_{RB}$  is the derivative of the rolling moment coefficient ( $C_R$ ) with respect to sideslip angle ( $\beta$ ), RANS solutions should be obtained under a sideslip condition. Results of the RANS solutions under the sideslip and without the sideslip condition are used to obtain the derivative of the rolling moment coefficient with respect to the sideslip by using the forward differencing method.

To determine which sideslip angle the suggested target value should be satisfied, military standards are used. Crosswind velocities for a landing approach in crosswind conditions are defined with corresponding levels in MIL-F-8785C military standards and shown in Figure 2.5 where trainer aircraft are Class IV [48].

**TABLE XI. Crosswind velocity.**

Level	Class	Crosswind
1	I	20 knots
and 2	II, III, & IV	30 knots
	Water-based airplanes	20 knots
3	All	one-half the values for Levels 1 and 2

Figure 2.5 Military standards MIL-F-8785C [48]

According to Figure 2.5, it is desired to have lateral stability up to 30 knots crosswind. For 0.186 Mach approach speed, this corresponds to 9.2 and 13.7 degrees

sideslips for 20 knots and 30 knots respectively. For simplicity, 10 degrees sideslip angle is selected for RANS solutions where  $C_{RB}$  is evaluated. As a result, the lateral stability constraint is shown in Table 2.8.

Table 2.8 The lateral stability constraint.

<b>Constraint</b>	<b>Altitude</b>	<b>Mach</b>	<b>Angle of Attack</b>	<b>Sideslip Angle</b>
$C_{RB} \leq -0.0004363$	Sea Level	0.186	8°	10°

It should be noted that  $C_{RB}$  is obtained by dividing  $C_R$  value at 10° sideslip angle to 10 by assuming the rolling moment is not created at 0° sideslip condition because the wing geometry is symmetric in the x-y plane and the angle of attack is not close to the stall region which can create roll moment due to flow separation.

In addition to the lateral stability and the maneuvering constraints, the wing reference area is constrained. According to the mission profile of the aircraft, the wing loading is determined at the beginning of a design process in the traditional approach [22].

The wing loading is an important design parameter that affects the performance of an aircraft. In this study, average wing loadings of the competitors are used and the corresponding wing area for 3298 kg is obtained as 16.21 m<sup>2</sup> which is also used as a reference area for calculation of the objective function and constraints previously. Therefore, the wing reference area constraint is defined in Table 2.9.

Table 2.9 The wing reference area constraint

<b>Constraint</b>
Wing Area = 16.21 m <sup>2</sup>

During the optimization, the taper ratio and the aspect ratio of the wing change because shape parameters vary. However, the weight of the wing is a function of the taper ratio and the aspect ratio due to the bending and torsion that the wing is

subjected to [22]. Hence, the taper ratio and the aspect ratio are also constrained in this study. To constrain the aspect ratio and taper ratio, competitor data are used which are shown in Table 2.10.

Table 2.10 The aspect ratio and the taper ratio of competitors.

<b>Parameter</b>	<b>KAI KT-1 Woongbi</b>	<b>Pilatus PC-21</b>	<b>Embraer EMB 314 Super Tucano</b>	<b>TAI Hurkus</b>
Aspect Ratio	6.96	4.65	6.67	6.23
Taper Ratio	0.46	0.54	0.43	0.44

According to Table 2.10, the aspect ratio and the taper ratio are limited above and below the bounds of competitors and determined without exceeding historical trends as shown in Table 2.11 [22].

Table 2.11 The taper ratio and the aspect ratio constraints.

<b>Constraint</b>
$0.3 < \text{Taper Ratio} < 0.6$
$4 < \text{Aspect Ratio} < 7.5$

As a result, evaluation of three different aerodynamic coefficients required for the objective function and constraints. Evaluation of  $C_D$  at 0.528 Mach and 0.1  $C_L$  for the objective function,  $C_L$  at 0.4 Mach for the maneuvering constraint, and  $C_{RB}$  at 0.186 Mach for the lateral stability constraint which are obtained with RANS solutions are required.

It should be noted that the horizontal tail design and the airfoil profile are as important as wing design for the longitudinal stability, and the vertical tail design is as important as the wing design for the directional stability [22]. Therefore, it is not possible to distinguish constraints of the wing optimization for the longitudinal and

the directional stability without considering the horizontal and the vertical tails. Hence, constraints are not defined for the pitching moment and the yawing moment coefficients that are related to the longitudinal and the directional stabilities in this study for the wing optimization.

## **2.6 Optimization Procedure**

As it is mentioned briefly in Chapter 1, there are different ways to perform an aerodynamic shape optimization. As it is also explained, it is aimed to perform the optimization by using surrogate models that are created as analytical functions that relate design parameters to the responses with the help of response surface methodology in this study. Methodologies of the different approaches to perform an aerodynamic shape optimization and advantages of the aerodynamic shape optimization using surrogate models will be discussed in the following paragraphs.

As mentioned, one of the possible ways to perform an aerodynamic shape optimization is to evaluate the gradient by obtaining RANS solutions at each optimization step to determine design parameter values at the next iteration step according to line search by starting from an initial wing geometry. This approach is a discrete aerodynamic shape optimization method that is gradient-based [33]. In this approach, the objective function and constraints should be evaluated by using RANS solutions at each optimization step. The line search algorithm uses gradient at each optimization step and gradient could be evaluated with the finite difference or adjoint methods.

If the finite difference method is used, since the gradient is also a function of aerodynamic coefficients, it requires perturbation of the grid. RANS solutions at perturbed grids should be obtained and used for gradient calculation. When the number of parameters increases, the finite difference method requires a high number of RANS solutions at each iteration step to calculate the gradient. Instead of the finite difference, the adjoint method could be used that does not require any additional

RANS solution for gradient calculation. An adjoint matrix solution is used to obtain sensitivities of aerodynamic coefficients with respect to the grid which can be used to calculate gradient analytically. Convergence of the adjoint matrix solution and evaluation of the gradient from sensitivities are challenging as well [34].

Another way of optimizing an aerodynamic shape could be using gradient-free optimization methods so-called gradient-free methods such as the genetic algorithm, the random search, and Nelder-Mead simplex algorithm when derivative information is unavailable, unreliable, or impractical to obtain [35]. Gradient-free algorithms are less likely to be stuck on local minimums compared to gradient-based methods. However, the convergence of the optimization is much slower [36].

As it is mentioned in the first paragraph that in this study, gradient-based optimization algorithms are used by replacing RANS solutions required for the calculation of the objective function, constraints, and gradient with high accuracy surrogate models.

One of the advantages of using surrogate models compared to other gradient-based optimization approaches is that it does not require any additional RANS solutions once a surrogate model is constructed. Therefore, the optimization process is much faster.

In gradient-based optimization methods, an optimization cycle is performed starting from the initial conditions. RANS solutions should be obtained at each optimization step for the objective function, constraint, and gradient calculations. However, when surrogate models are used to replace RANS solutions, additional RANS solutions are not required when optimization starts from a different initial condition, the analytical functions are used instead of RANS solutions. Therefore, surrogate model based optimizations are more flexible to change initial conditions or constraints. Also, surrogate model based optimizations are advantageous for searching global minimums compared to discrete gradient-based optimization methods.

However, constructing a high accuracy surrogate model is challenging because it may require much more RANS simulations compared to other optimization approaches. The number of RANS solutions obtained to construct a surrogate model depends on the data set used to fit the model.

Data set can be considered as the values of the objective function and constraints obtained at the design points among the defined design space. In this study, the design space is a multidimensional combination and interaction of input variables (i.e., design parameters, wing shape parameters, optimization variables) [37]. Each combination of design parameters in the design space is called as design points. It is important to determine design points because each design point requires RANS simulations to evaluate responses and the distribution of design points affects the surrogate model accuracy.

A high number of design points increases the accuracy of the surrogate model but the number of RANS simulations as well. Therefore, the design of experiment techniques are used to determine design points. In this study, it is aimed to achieve a high accuracy surrogate model while decreasing the number of RANS simulations compared to the traditional design of experiment approaches. For this purpose, the sequential experimentation technique is used in this study.

Sequential experimentation is any procedure where the choice of a further design increment depends upon previous data [38]. Details of the sequential experimentation technique followed in this study are explained in Chapter 4. All details related to the design of experiments, response surface methodology, and RANS solutions are explained in Chapters 3 and 4. The optimization process followed in this study with the explained approaches is shown as a flowchart briefly in Figure 2.6.

As it could be observed from Figure 2.6 that optimization starts with the design of the experiment part. Since the sequential experimentation technique is used, it is an iterative procedure that updates the design points according to the statistical analyses obtained after RANS solutions.

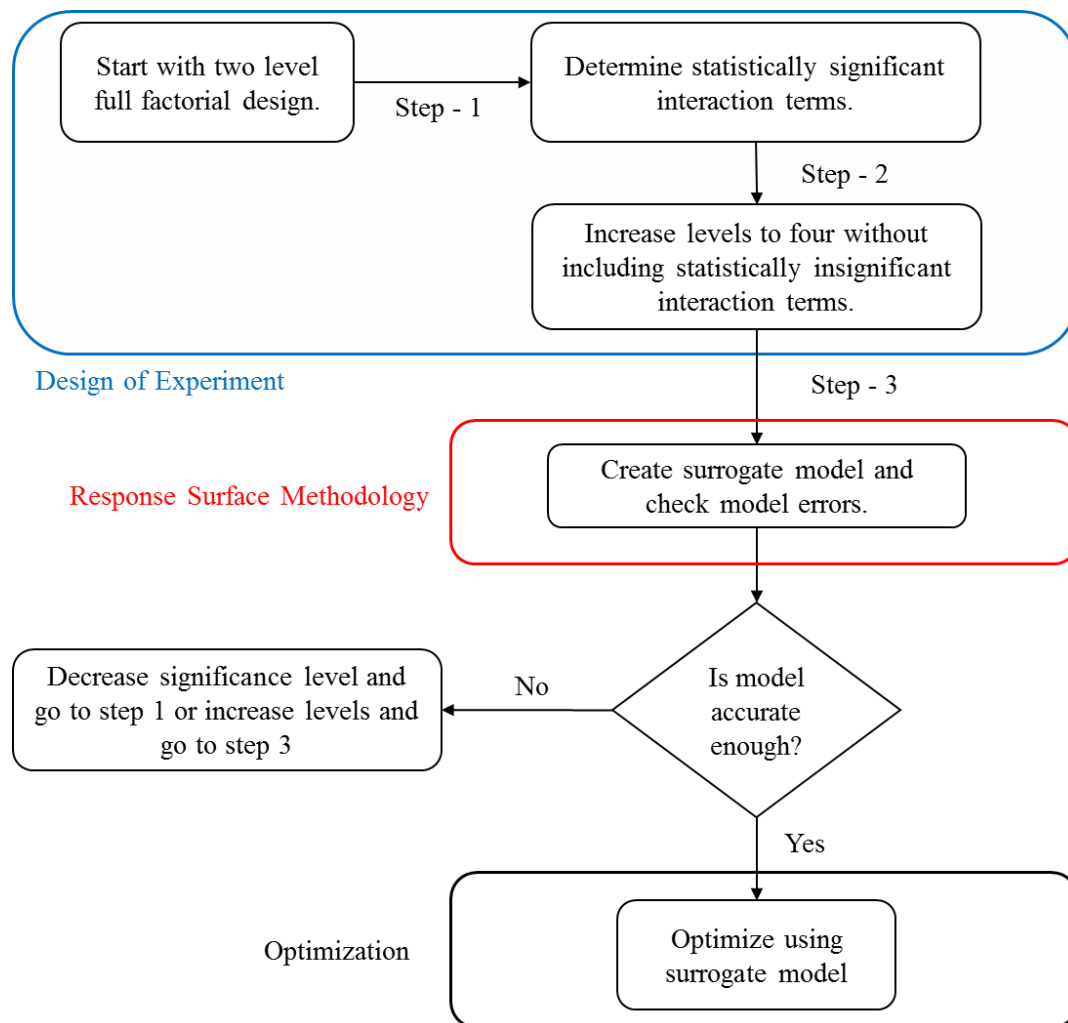


Figure 2.6 Optimization process flowchart.

First, a traditional 2-level full factorial design is constructed in this study. The two-level full factorial design is advantageous to identify important design parameters at the start of a response surface study [39]. Two-levels are selected as the maximum and minimum values of the parameters obtained in Chapter 2.

After obtaining responses which are aerodynamic coefficients used in the objective function and constraints for the two-level full factorial design, statistical analyses are performed to determine statistically significant interaction terms and the methodology is explained in detail in Chapter 4.

Statistically significant parameters are parameters that the significance of a parameter is tested and accepted with a statistical approach. Observed data is compared with a claim, the truth of which is being assessed is a test of significance that is a formal process [40].

In this study, the claim is that the effect of a parameter or interaction between other parameters is significant in terms of the response change. According to the statistical analyses performed after step one shown in Figure 2.6, interaction terms that are not statistically significant are eliminated. The experiment design is updated from two-level full factorial to four-level full factorial, but design points corresponding to the interaction of insignificant interaction terms are not included after step two as shown in Figure 2.6.

It is selected to achieve four levels in this study because it is expected to have at least third order and nonlinear relations between responses and design parameters. RANS solutions are obtained for additional design points after the design of the experiment is updated. With the help of response surface methodology, analytical surrogate models are created after step three in Figure 2.6.

The constructed surrogate model is examined in terms of model accuracy. RANS solutions are obtained for randomly selected points from the design space and results are compared with the surrogate model results. It should be noted that randomly selected points are not added into the designed experiment. According to the errors of the surrogate model, it should be decided to accept the accuracy of the surrogate model or update the design space to increase the accuracy.

If the surrogate model is not accurate enough, two different approaches could be followed. One of them is to decrease the significance level which will cause some of the insignificant interaction terms to be significant. After that, the design space will be updated by including factorial design points of the additional statistically significant interaction terms that arise due to a decrease in the significance level. Another way is to increase the number of levels furthermore to capture the curvature of the response surface to be modeled by increasing the order of the function.

In both ways, after updating the design of the experiment, RANS solutions should be obtained and a surrogate model should be constructed. Iteratively, the design space and surrogate models are updated until the desired accuracy is reached.

Starting from a two-level full factorial design, the number of design points is increased until the desired accuracy is achieved. While increasing the number of design points, previous design point results are also used to construct surrogate models.

After surrogate models are validated by comparing the results of the surrogate models with RANS solutions, surrogate models could be used in the optimization. Since surrogate models used to calculate aerodynamic coefficients in the objective function and constraints are nonlinear functions, nonlinear constrained optimization is performed with the algorithms explained in Section 2.7.

After the optimization is completed and the optimum configuration is obtained, the optimum and the initial wings are compared in terms of the objective function value obtained from RANS solutions because surrogate models include model error. Also, the suitability of the optimum wing to the constraints is examined to validate the optimum wing. After the optimum wing is validated, the study is successfully completed.

## **2.7 Optimization Algorithms**

In this study, MATLAB software is used for optimization which has optimization libraries that could be used easily [49]. As it is explained in Section 2.5, the equality and the inequality constraints are required for the optimization and the objective function and constraints are nonlinear functions. Therefore, MATLAB's "fmincon" function is used to perform the optimization with nonlinear constraints [49].

There are different algorithms implemented in MATLAB for solving optimization problems with nonlinear objective functions and constraints. In this study, sequential

quadratic programming (SQP) and interior-point algorithms implemented in MATLAB are used.

In the sequential quadratic programming algorithm, quadratic programming subproblems are generated in each iteration that is used to form a search direction. The search direction is used in a line search process that uses an approximation of the Hessian of the lagrangian. The Hessian is approximated using the BFGS method which is a popular method [50]. When problems include significant nonlinearities in constraints, sequential quadratic programming shows its strength [51].

In the interior-point algorithm, a sequence of approximate minimization problems are solved. The approximate problem sequence is a sequence of equality constrained problems that is easy to solve compared to inequality constraints. The approximation is performed by using slack variables and a barrier function. To solve the approximate problem, the algorithm first attempts to take a direct step, a Newton step, which attempts to solve the Karush-Kuhn-Tucker (KKT) equations using the Hessian of the function [50]. If the direct step is not successfully performed, a conjugate-gradient step using a trust-region algorithm is performed [50]. Interior-point is advantageous for large, sparse problems because the algorithm works faster when linear algebra is required.

Optimization is performed by using SQP and interior-point algorithms to observe the effect of the optimization algorithm on the optimum geometry and results are presented in Chapter 5.



## CHAPTER 3

### FLOW SOLUTIONS WITH SU2

In this chapter, the theoretical background of flow solutions is clarified. As mentioned, Reynolds-averaged Navier-Stokes equations are solved in this study to obtain aerodynamic coefficients. First, governing equations, solution procedures, and boundary conditions are explained in detail. After that, a grid dependency study performed to determine grid size and brief information about the scripts used to obtain RANS solutions are presented.

#### 3.1 Governing Equations

Stanford University Unstructured (SU2) flow solver which is an open-source software is used to perform flow solutions in this study [52]. Reynolds-averaged Navier-Stokes (RANS) equations are solved using SU2 with the finite volume method. Navier-Stokes equations are the mathematical definition of a compressible flow that includes conservation of the mass, the momentum, and the energy.

Compressible Navier-Stokes equations can be expressed in differential form as shown in Equation (2) [53].

$$\frac{\delta U}{\delta t} + \nabla \cdot \bar{F}^c(U) - \nabla \cdot \bar{F}^v(U, \nabla U) - S = 0 \quad (2)$$

Where  $U$  is the vector of conservative variables defined in Equation (3).

$$U = \{\rho, \rho \bar{v}, \rho E\}^T \quad (3)$$

Where  $\rho$  is the density,  $\bar{v} = \{u, v, w\}^T$  is the velocity composed of  $u, v, w$  which are velocities in  $x, y,$  and  $z$  directions respectively, and  $E$  is the total energy per unit mass.  $S$  is defined as a generic source term and convective and viscous fluxes are defined in Equations (4) and (5) respectively.

$$\bar{\mathbf{F}}^c = \left\{ \begin{array}{c} \rho \bar{\mathbf{v}} \\ \rho \bar{\mathbf{v}} \times \bar{\mathbf{v}} + \bar{\mathbf{I}} p \\ \rho E \bar{\mathbf{v}} + p \bar{\mathbf{v}} \end{array} \right\} \quad (4)$$

$$\bar{\mathbf{F}}^v = \left\{ \begin{array}{c} \dot{\bar{\tau}} \\ \bar{\tau} \cdot \bar{\mathbf{v}} + \kappa \nabla T \end{array} \right\} \quad (5)$$

The term  $\kappa$  is the thermal conductivity,  $T$  is the temperature, and  $p$  is the static pressure. Stress tensor,  $\bar{\tau}$ , is shown in Equation (6).

$$\bar{\tau} = \mu(\nabla \bar{\mathbf{v}} + \nabla \bar{\mathbf{v}}^T) - \mu \frac{2}{3} \bar{\mathbf{I}} (\nabla \cdot \bar{\mathbf{v}}) \quad (6)$$

Where  $\mu$  is the viscosity. The perfect gas assumption is made to close the systems of equations by solving the equation of state.

To include the turbulence, Reynolds decomposition is performed in which the instantaneous quantity of the variables due to the turbulence are divided into their time-averaged and fluctuating quantities. Variables defined in the Navier-Stokes equation are replaced with the time-averaged and fluctuating quantities of the variables and due to fluctuation terms in the velocity, an additional stress term appears to be solved in the momentum equations called the Reynolds stress. To solve the Reynolds stresses, a turbulence model is used and the system of equations is called as Reynolds-averaged Navier-Stokes equations. RANS equations are widely used for compressible and turbulent flows.

In SU2 partial differential equations (PDEs) are discretized by using the finite volume method with a standard edge-based structure on a dual grid and a vertex-based scheme is used to construct control volumes [53]. Cells that share the particular node are connected to form median-dual control volumes. Differential form of the Navier-Stokes equation is converted to integral form by using the Reynolds Transport theorem and the integral form of the Navier-Stokes equations is given in Equation (7) [54].

$$\int_{\Omega_i} \frac{\partial \mathbf{U}}{\partial t} d\Omega + \sum_{j \in \mathbf{N}(i)} (\bar{\mathbf{F}}_{ij}^c + \bar{\mathbf{F}}_{ij}^v) \Delta S_{ij} - \mathbf{Q} |\Omega_i| = 0 \quad (7)$$

Convective and viscous fluxes are projected into local and normal directions of the edge and  $\Delta S_{ij}$  is the area of the associated face with the edge “ij”. The term  $|\Omega_i|$  is the volume of the dual control volume and  $N(i)$  is the set of neighboring nodes to node “i”. Equation (7) could be expressed furthermore (8) as:

$$\int_{\Omega_i} \frac{\partial \mathbf{U}}{\partial t} d\Omega + R_i(\mathbf{U}) = 0$$

Where  $R_i(\mathbf{U})$  is the numerical residual in Equation (8).

### 3.2 Flux Discretization

The convective and viscous fluxes are evaluated at the midpoint of an edge. SU2 has different schemes for convective flux discretization which are Jameson-Schmidt-Turkel (JST), Roe, AUSM, HLLC, and Roe-Turkel. In this study, the JST convective flux splitting method which is a central scheme is used. The JST flux splitting method is effective for steady-state calculations in a wide Mach range [55]. In addition, the JST method offers improved stability of the centered scheme [56].

To evaluate viscous fluxes, the first derivatives of the flow quantities are required and derivatives could be calculated by using the Green-Gauss, or the least squares methods in SU2. In this study, the least squares method is used to calculate derivatives.

### 3.3 Time Integration

Integration of time term in Equation (8), implicit integration method is used. Equations are linearized about the current state to obtain a linear system to be solved which is shown in Equation (9).

$$\left( \frac{|\Omega_i|}{\Delta t_i^n} \delta_{ij} + \frac{\delta R_i(\mathbf{U}^n)}{\delta U_j} \right) \cdot \Delta U_j^n = -R_i(\mathbf{U}^n) \quad (9)$$

The next solution step is achieved by updating the current state as shown in Equation (10).

$$\Delta U_i^n = U_i^{n+1} - U_i \quad (10)$$

Linear solvers are implemented in SU2 to solve Equation (9). Krylov subspace methods such as the generalized minimal residual and biconjugate gradient stabilized methods could be used to solve linearized systems implicitly. In this study, a flexible generalized minimal residual method is used for the implicit solution.

### **3.4 Turbulence Model**

In SU2, turbulence modeling is based on the Boussinesq hypothesis which states that the turbulence effect could be represented as an increased viscosity which allows dividing viscosity into the turbulent and the laminar components [54]. Turbulence models are used to obtain a suitable turbulent viscosity using the flow state and the model equations are solved for a new set of variables [53].

The Spalart-Allmaras model is one of the most common and widely used one equation turbulence model [53]. The Spalart-Allmaras model demonstrates acceptable results for the solution of the adverse pressure gradient and boundary layers. In addition, since it is a one equation model, the computation time is less and converges faster compared to two-equation models [57]. Therefore, in this study, the Spalart-Allmaras turbulence model is used.

### **3.5 Boundary Conditions**

For a boundary region that is far away from the source of a disturbance where flow is being uniform, a far-field boundary condition is used. [58]. The far-field boundary is located approximately 20 body lengths away from the trailing edge [53]. At the wing surfaces, a no-slip boundary condition is used satisfies that the fluid is stationary at the solid boundary of the wing. In addition, around the wing, the grid is

refined to capture the flow gradient due to adverse pressure gradient, wake, and possible flow separations. Boundary conditions used in this study are shown in Figure 3.1 from a cross-sectional view of the grid. Also, the refined grid region is shown in Figure 3.1.

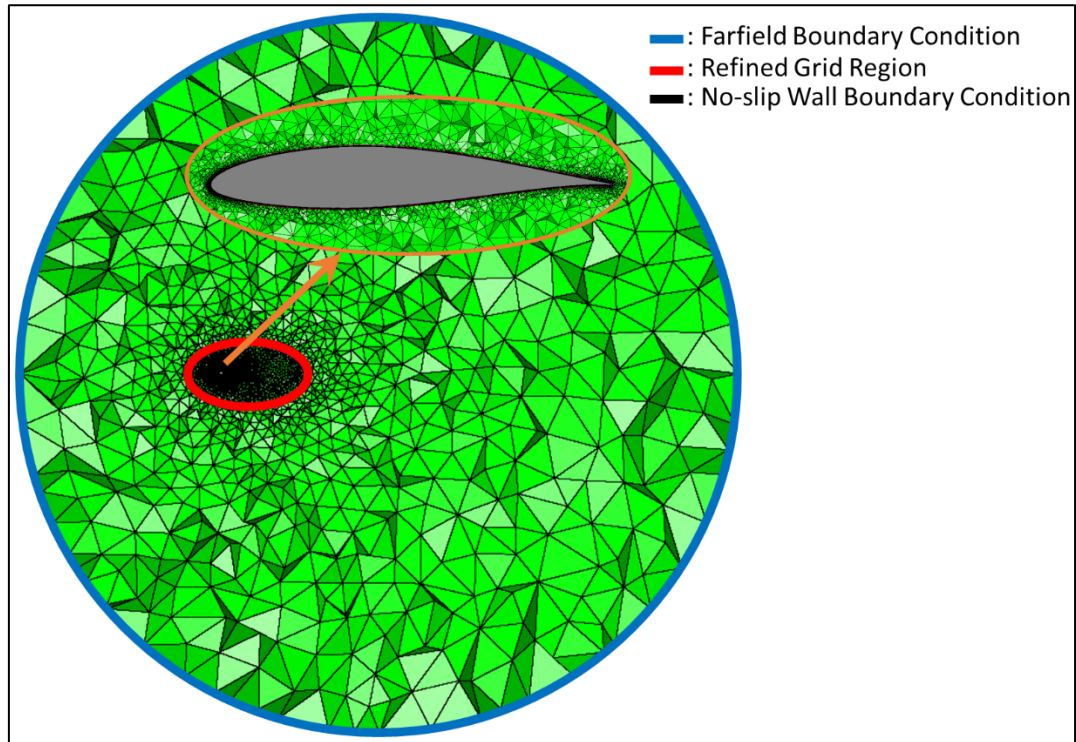


Figure 3.1 Boundary conditions and refined grid region.

### 3.6 Flow Solutions at the Constant Lift Coefficient

The SU2 provides a so-called “fixed  $C_L$ ” solution option to allow users to be able to obtain flow solutions at a target lift coefficient. When this option is turned on, the solver updates the angle of attack during the solution until the target lift coefficient is satisfied. In this study, in order to minimize the drag coefficient at a constant lift coefficient, this option is employed in the flow solutions used to form response surfaces.

### 3.7 Grid Generation and Mesh Dependency

The grid used in this study is a hybrid-type grid that is composed of tetrahedral and prismatic elements generated with Pointwise software [59]. Prismatic elements are used in the boundary layer region to satisfy  $y^+ \approx 1$  for resolving viscous sublayer without wall functions [53]. Tetrahedral cells are used in the rest of the domain to fulfill prism cells and far-field boundaries.

The thickness of the prism cells is determined by approximating the boundary layer thickness. The boundary layer thickness is approximated by calculating the boundary layer thickness of a flat plate for turbulent flow. The boundary layer thickness of a turbulent flow through a flat plate could be calculated by using Equation (11) [60]:

$$\frac{\delta}{x} \cong \frac{0.38}{(\text{Re})^{1/5}} \quad (11)$$

From Equation (11), the maximum boundary layer thickness among the design space boundaries is approximated as 3 cm. Therefore, the height of the boundary layer grid is fixed for all geometries to 3 cm and the first layer height is adjusted to achieve  $y^+ \approx 1$  for all geometries.

The growth rate of prism cell layers is fixed to 1.2 and the number of layers is adjusted accordingly to achieve the approximated total boundary layer thickness. The hybrid-grid structure is shown in Figure 3.2, where prism cells are marked with red color and tetrahedral cells are marked with green color.

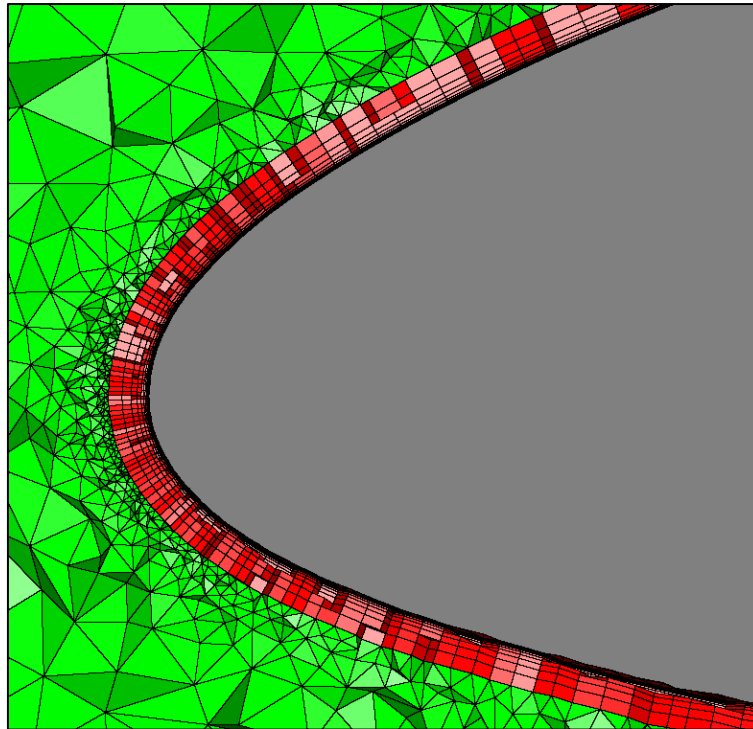


Figure 3.2 Cross-sectional view of the grid.

Boundary layer grids are generated according to the previous studies performed to validate SU2 solver and the theoretical background [53]. Therefore, a grid dependency study is performed to observe the effect of grid points on the airfoils at the root and tip only.

A different number of grid points are distributed on the root and tip airfoils which affects the airfoil and the wing leading edge curvatures. Six different grids are generated with the different number of grid points on the root and the tip airfoils which are shown in Figure 3.3.

In Figure 3.3, grids are shown from the coarse grid to the fine grid starting from the top to the bottom respectively. The same number of grid points is used for the tip and the root airfoil profiles. The coarsest grid has 26 and the finest grid has 456 grid points on each of the root and the tip airfoils. Aerodynamic coefficients used in the objective function and constraints are obtained for different grids at the

corresponding flow conditions. Results of RANS solutions obtained with different grids are compared to observe the grid effect on the solution (Figure 3.4-3.6).

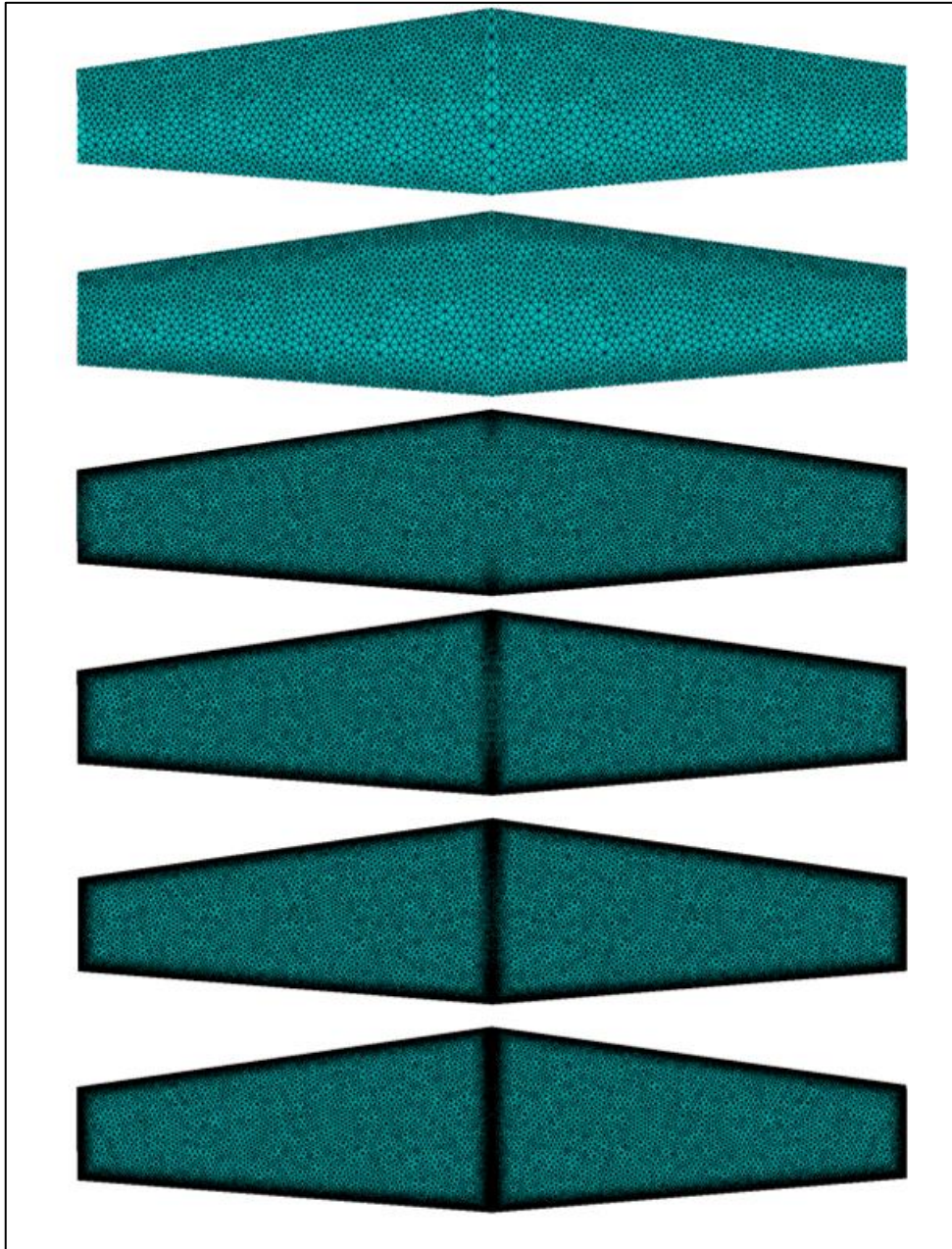


Figure 3.3 Grids generated with a different number of grid points at the root and tip airfoils.

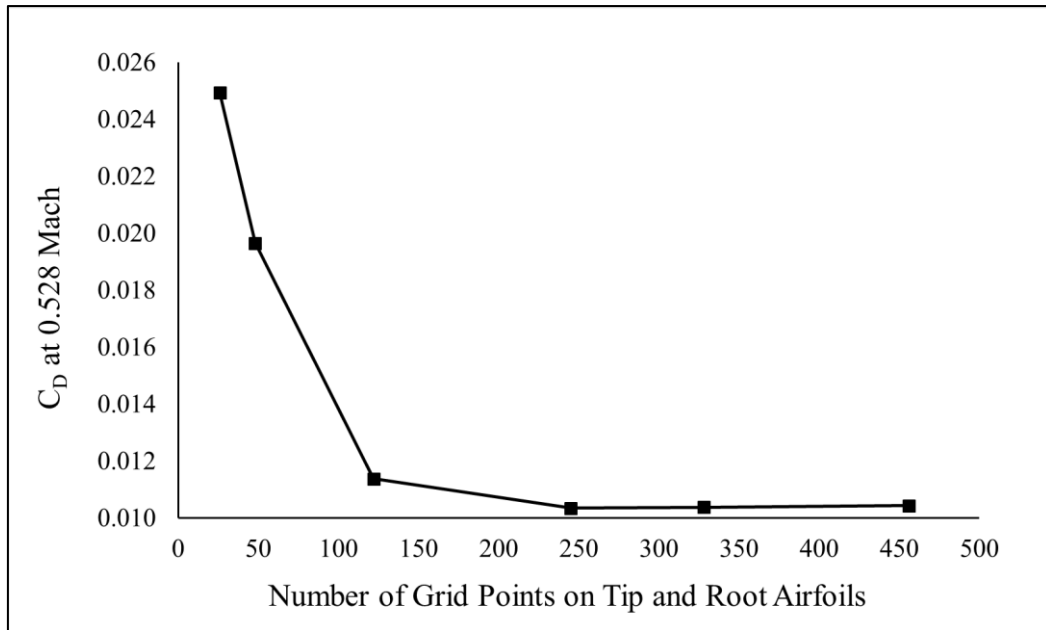


Figure 3.4  $C_D$  at 0.528 Mach for different number of grid points on the tip and the root airfoils

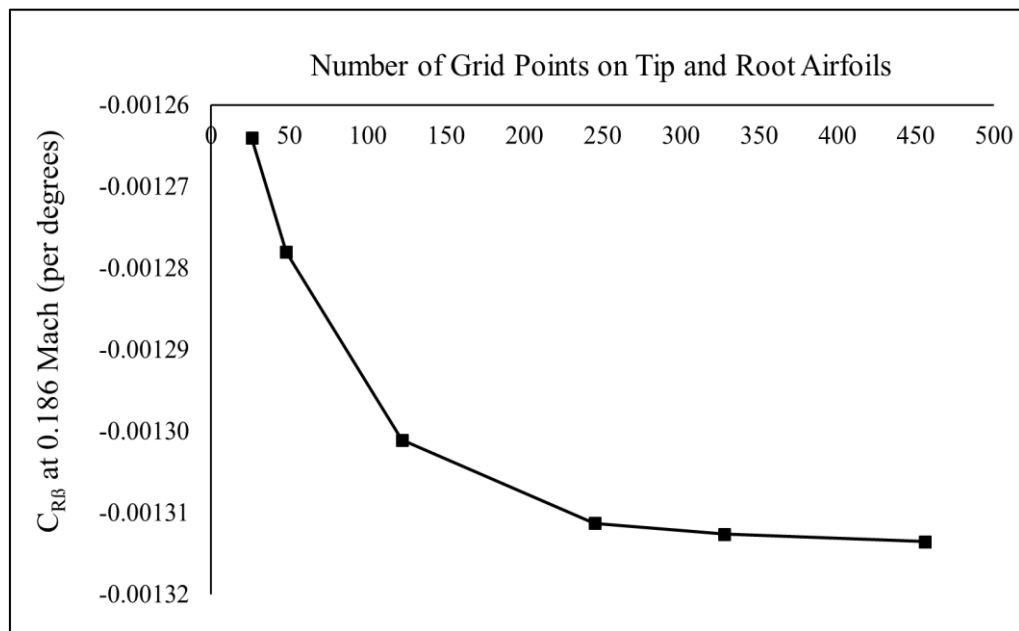


Figure 3.5  $C_L$  at 0.528 Mach for different number of grid points on the tip and the root airfoils

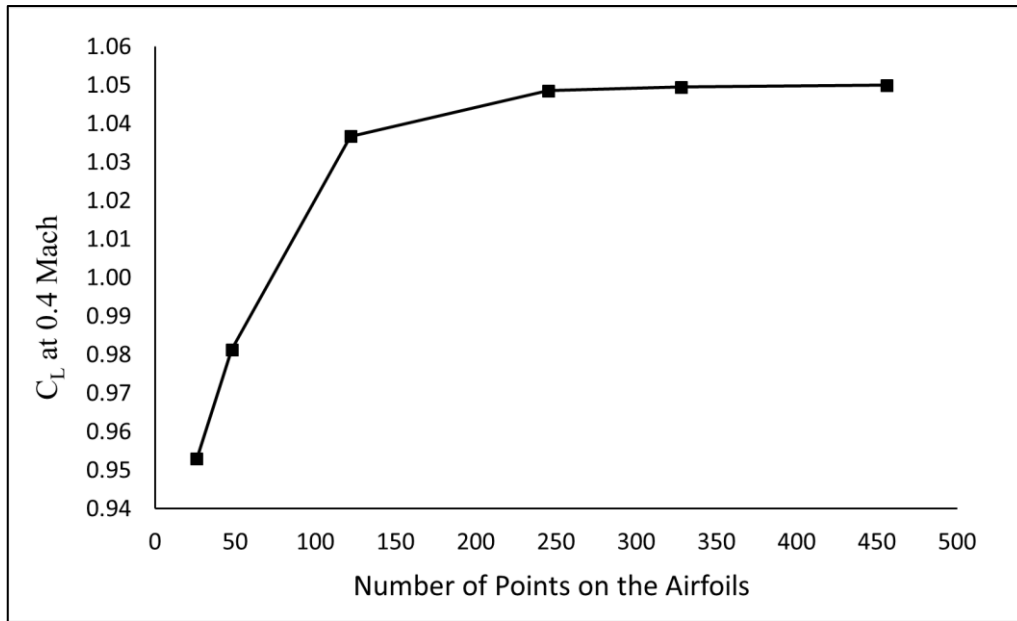


Figure 3.6  $C_{RB}$  at 0.186 Mach for different number of grid points on the tip and the root airfoils

According to figures 3.4 - 3.6 coefficients converge to the same value after 250 grid points are used on each of the tip and the root airfoils. Hence, in this study, 250 grid points are used for the root and the tip airfoils. The number of cells in the domain for the wings among the design space is approximately between 3 to 6 million.

### 3.8 Flow Solution Scripts

It is required to obtain RANS solutions for different wing geometries corresponding to a design point. Since the number of design points might be in the order of hundreds, it is not possible to obtain RANS solutions one by one manually. Therefore, python scripts are coded to obtain RANS solutions for different wing geometries automatically.

Wing geometries are generated by using the Rhinoceros CAD tool [32]. Rhinoceros allows users to generate automated CAD geometries with its python libraries. It has its python compiler that compiles python scripts including its libraries to generate CAD geometries. Python scripts are generated to create wing geometries

corresponding to defined design parameters automatically to be used in the grid generation process.

Grids of the different wing geometries are created with Pointwise meshing software [59]. Pointwise allows the user to generate a grid using its scripting language “glyph”. Python scripts are coded to generate a “glyph” for the automated grid generation process.

RANS simulations are also performed by using a python script that automatically performs SU2 simulations for each wing geometry. The reference area and the point where aerodynamic moments are calculated, the quarter chord of the mean aerodynamic chord, are different for each wing geometry. The script calculates the reference area and the moment point for each geometry and obtains RANS solutions accordingly.



## CHAPTER 4

### RESPONSE SURFACE METHODOLOGY

The response surface methodology is used to develop, improve, and optimize a process, which is a collection of statistical and mathematical techniques [39]. In this section, the design of experiment techniques applied, methods for determining significant design parameters, and creating surrogate models are explained in detail.

#### 4.1 Full Factorial Designs

Factorial designs are widely used for experiments in which several factors are involved to investigate the main and interaction effects of the factors on the response [39]. These designs are also called screening designs which are basically generated to examine the effects of main factors and interactions among them.

The interaction effect is an effect of one variable that depends on the value of another variable and vice versa. In other words, the interaction effect could be considered as an effect that occurs when a variable has a different effect on the response depending on the value of the other variable. To be able to examine the interaction effects, the difference in the response due to the change of a factor at different levels of another factor should be calculated. Hence, factorial designs are essential to examine the main factor and interaction effect.

In this study, a full factorial design is conducted to examine the effect of all main factors and all of their interactions. A two-level full factorial design is conducted for six design parameters which have  $2^6 = 64$  design points (i.e., wing configurations). It includes each possible combination of parameters. Levels are assigned as the minimum and the maximum possible values of the parameters.

## 4.2 Determination of Significant Design Parameters

After responses are obtained for two-level full factorial design, significant main factors and their interactions on responses could be determined with statistical methods. In this study, Minitab software is used to determine significant design parameters on each response [61].

In an experimental procedure, design points are replicated to calculate pure error that is due to the experimental procedure, the setup accuracy, or the physics of the experiment. This is achieved by performing an experiment on the same design point from a scratch and obtaining the difference in the response. However, for numerical calculations, it is not possible to achieve. For RANS solutions which is a numerical calculation when the same numerical methodology and grid is used, the response is the same. Hence, pure error calculation is not possible for RANS solutions.

The pure error of the experiment is important because it helps to understand whether the change of the response due to the change of a parameter is important or within error tolerances (i.e., negligible). The degree of freedom of the pure error is equal to the number of replicated design points minus one [62]. In this study, since RANS solutions are used, the degree of freedom of the error is zero.

Minitab uses Lenth's pseudo standard error (PSE) to identify important effects if the error term has zero degrees of freedom as it is in this study [63]. Minitab plots Pareto charts for the absolute effect of each main factor and the interaction and draws a line at the margin of error. The margin error is calculated by using the Lenth's pseudo standard error value [64]. The line is drawn at the margin of error and main factors and interaction terms with an absolute effect value above the margin of error are assumed statistically significant [65].

Significance level ( $\alpha$ ) should be determined for the calculation of the margin error. The significance level is the risk of saying that a factor is significant when in fact it is not [65]. In this study, the significance level is taken as 0.05 which corresponds to

the %5 risks of saying that a factor is significant when in fact it is not. The margin of error could be calculated by using Equation (12).

$$\text{The margin of Error} = t * \text{Pseudo Standard Error} \quad (12)$$

Where t is the  $1 - \alpha/2$  quantile of a t-distribution. The pseudo standard error could be calculated by following the steps shown in Table 4.1.

Table 4.1 Calculation steps of the Lenth's pseudo standard error.

Step	Calculation
1	Calculate absolute value of the effects
2	Calculate 1.5 times the median of the effects calculated in Step 1
3	Calculate the median of the effects that are less than 2.5 times the value calculated at Step 2
4	Calculate pseudo standard error which is 1.5 times the median calculated in Step 3

By comparing the absolute effect value with the margin of error, the main and the interaction terms that have a significant effect are obtained.

### 4.3 Regression Model

The regression model is the mathematical relationship between design parameters and the response. In this study, a higher-order multiple linear regression model is used and constructed by using Minitab software [39].

An example of a second-order multiple linear regression model for two predictors (i.e, design variables, parameters) is shown in Equation (13).

$$y = \beta_0 + \beta_1x_1 + \beta_2x_2^2 + \beta_{11}x_1^2 + \beta_{22}x_2^2 + \beta_{12}x_{12} + \varepsilon \quad (13)$$

In Equation (13),  $y$  is the response,  $x_1$ , and  $x_2$  are the main factors and  $x_{12}$  is the interaction term. The term  $\varepsilon$  stands for the error of the model and  $\beta$  terms are called regression coefficients.

Equation (13) is in linear form and more than one parameter is used to predict response. Since the order of the function is two, it is a second-order multiple linear regression model. It is possible to omit interaction terms or change the order to construct the model. Minitab could create the model by including any of the parameters in any order as soon as it is in the linear form.

For each response and a predictor value, the model should satisfy the minimum error. Therefore, predictor coefficients should be obtained to satisfy the minimum model error defined as  $\varepsilon$  in Equation (13). Since the value of the design parameters and responses are known, only unknowns are predictor coefficients that minimize the error. Minitab uses the ordinary least square method for the evaluation of coefficients to form the function.

In the least-squares method, linear system equations are denoted in matrix form as Equation (14).

$$\mathbf{y} = \mathbf{X}\beta + \varepsilon \quad (14)$$

The term  $y$  is a  $n \times 1$  vector where  $n$  is the number of design points that correspond to the response at each design point.  $X$  is a  $n \times p$  model matrix consisting of the levels of the independent variables,  $\beta$  is a  $p \times 1$  vector of the regression coefficient to be solved and  $\varepsilon$  is the  $n \times 1$  error term matrix. The solution could be obtained for  $\beta$  vector to minimize  $\varepsilon$  as shown in Equation (15).

$$\mathbf{b} = (\mathbf{X}'\mathbf{X})^{-1} + \mathbf{X}'\mathbf{y} \quad (15)$$

The term  $b$  is the solution of regression coefficients  $\beta$ .

In this study, the regression model is started from a first-order linear model including all interactions and then improved by including higher-order terms and removing

interaction terms with a small effect on the response according to their coefficient values.

#### 4.4 Validation Process of the Model

During the construction of the model starting from a simple first-order linear model with interaction terms, adjusted R-square values are examined. According to the adjusted R-square value, until the desired value is reached, the model is updated by increasing order and removing unnecessary interaction terms according to coefficient values in Minitab.

Calculation of the adjusted  $R^2$  is given in Equation (16).

$$R_{\text{adjusted}}^2 = 1 - \frac{(1 - R^2)(N - 1)}{N - p - 1} \quad (16)$$

Where  $R^2$  is the regular  $R^2$ ,  $N$  is the total number of design points and  $p$  is the design variables in the equation. Regular  $R^2$  could be calculated by using Equation (17).

$$R^2 = 1 - \frac{\sum(y_i - \hat{y}_i)^2}{\sum(y_i - \bar{y})^2} \quad (17)$$

Where  $y_i$  is the actual response,  $\hat{y}_i$  is the model response and  $\bar{y}$  is the mean of the responses.  $R^2$  could be ideally 1 where the model has no error.

It is generally desired to have  $R^2$  value higher than 0.9. However, when the number of design points increases  $R^2$  also increases which might be deceptive. Therefore, it should be adjusted according to the number of design points, which is the adjusted  $R^2$ , and adjusted  $R^2$  is observed during the construction of the model in this study. A value for the adjusted  $R^2$  above 0.95 is accepted in this study.

After the regression model is constructed with desired adjusted  $R^2$  value, RANS solutions are obtained for wings with randomly selected design parameters. Randomly selected design points are not used to fit the regression model and selected within the design space. The results of the RANS solutions are compared with the

model results to observe the accuracy of the model. According to the relative error between RANS solutions and the model, the model is accepted.

## CHAPTER 5

### RESULTS AND DISCUSSION

In this section, the results of the two-level full factorial design are discussed first. After that, using the results of the two-level full factorial design, statistically significant interaction terms are determined and design points are updated. Constructed surrogate models are validated by comparing the results of the analytical functions with the RANS solutions. The effect of the airfoil profile on the optimization process is presented. Several optimizations are performed with different optimization algorithms and initial conditions to observe the effect of optimization algorithms and initial conditions on the optimization. The optimum configuration is validated by comparing against the RANS solutions. In addition, the suitability of the optimum configuration to the constraints is also examined. The results obtained are discussed in detail.

#### 5.1 Two-Level Full Factorial Design

Surrogate models used in the optimization relate a response to the optimization variables in the form of an analytical function. Therefore, a surrogate model should be constructed for each response. Responses are the aerodynamic coefficients used in the objective function and the constraints. The drag coefficient while keeping the lift coefficient constant as 0.1 at  $M_\infty = 0.528$  is the response of the objective function. The drag coefficient at the constant  $C_L = 0.1$  is obtained by using the fixed  $C_L$  solution mode of the SU2. The lift coefficient at  $M_\infty = 0.4$  and  $AoA = 10^\circ$ , and the rolling moment coefficient at  $M_\infty = 0.186$ ,  $AoA = 8^\circ$ , and  $AoS = 10^\circ$  are the responses required in the maneuvering and the lateral stability constraints. As a result, three different surrogate models are required in the optimization.

The design of the experiment starts with the two-level full factorial design that corresponds to 64 design points. For three responses, 64 design points require 192 RANS solutions. According to the solutions, responses are observed to determine whether constraints are feasible or not. To observe the feasibility of the maneuvering constraint, values of the lift coefficient are plotted for each wing geometry, design point, and shown in Figure 5.1.

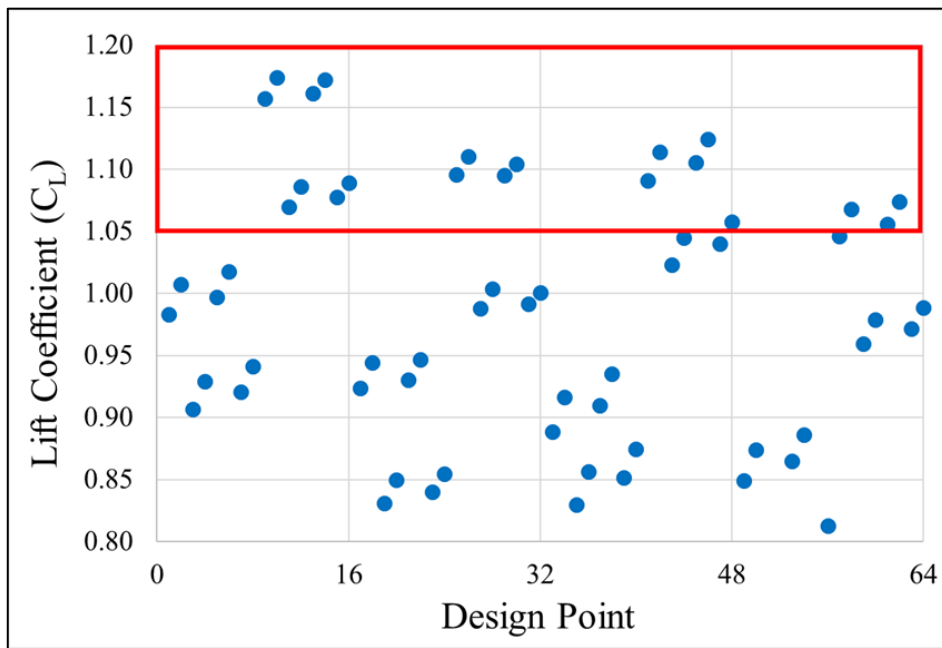


Figure 5.1 The lift coefficient ( $C_L$ ) value of the geometries in design space.

In Figure 5.1, the area shown with red rectangular borders is the area where the maneuvering constraint is satisfied which corresponds to the  $C_L$  value higher than 1.05. Therefore, it could be stated that the maneuvering constraint is feasible and the optimum design that satisfies the maneuvering constraint can be achieved.

To observe the feasibility of the lateral stability constraint, values of the rolling moment coefficient change with respect to sideslip angle,  $C_{RB}$ , are plotted for each wing geometry and shown in Figure 5.2.

In Figure 5.2, the area shown with red rectangular borders is the area where the lateral stability constraint is satisfied which corresponds to  $C_{RB}$  value less than -0.0004363.

Therefore, it could be stated that the lateral stability constraint is feasible and the optimum design that satisfies the lateral stability constraint can be achieved.

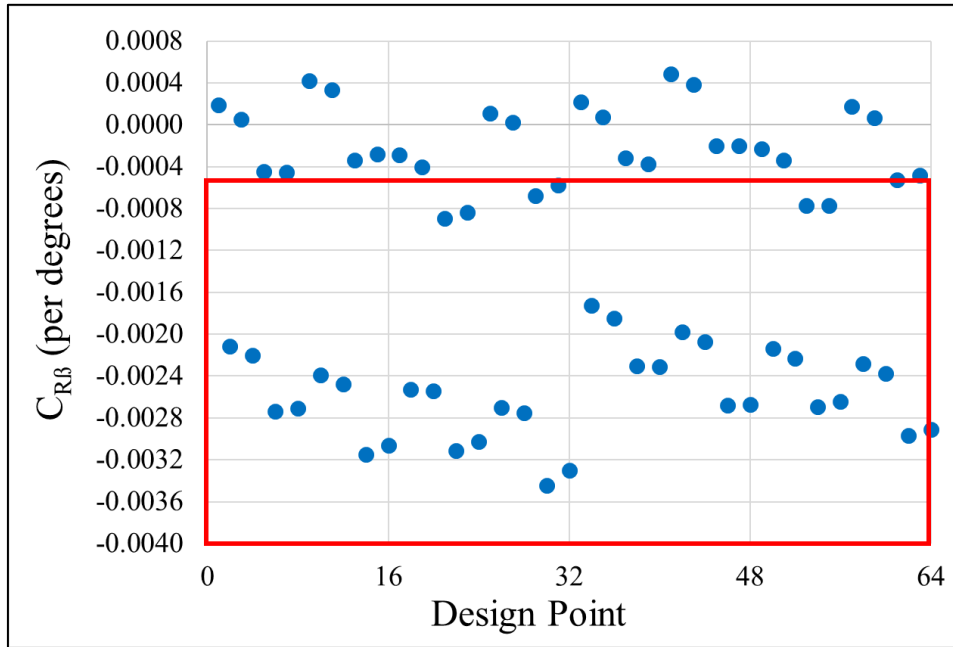


Figure 5.2 The rolling moment change w.r.t. sideslip angle ( $C_{RB}$ ) value of the geometries in design space.

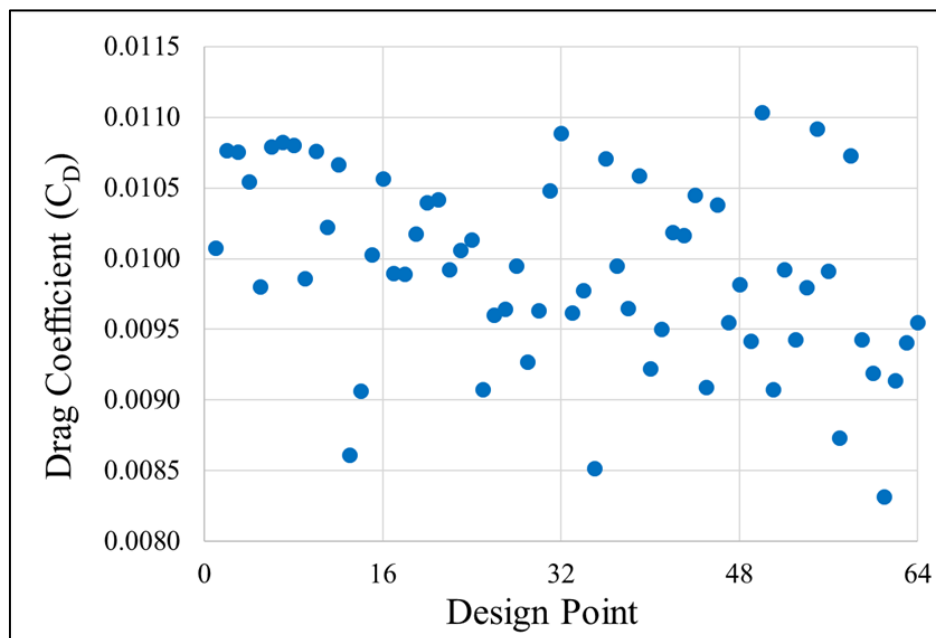


Figure 5.3 The drag coefficient ( $C_D$ ) at 0.1 lift coefficient ( $C_L$ ) value of the geometries in design space

In addition, values of the objective function which is the drag coefficient,  $C_D$ , are plotted for each wing geometry and shown in Figure 5.3. The optimum design will be the one that has the lowest possible drag coefficient among the values shown in Figure 5.3 that satisfies conditions shown with red area in Figure 5.1 and Figure 5.2.

## 5.2 Determination of Statistically Significant Parameters

After RANS solutions are obtained for the two-level full factorial design, interaction terms that have a significant effect on each response are obtained by using Minitab as explained in Chapter 4.

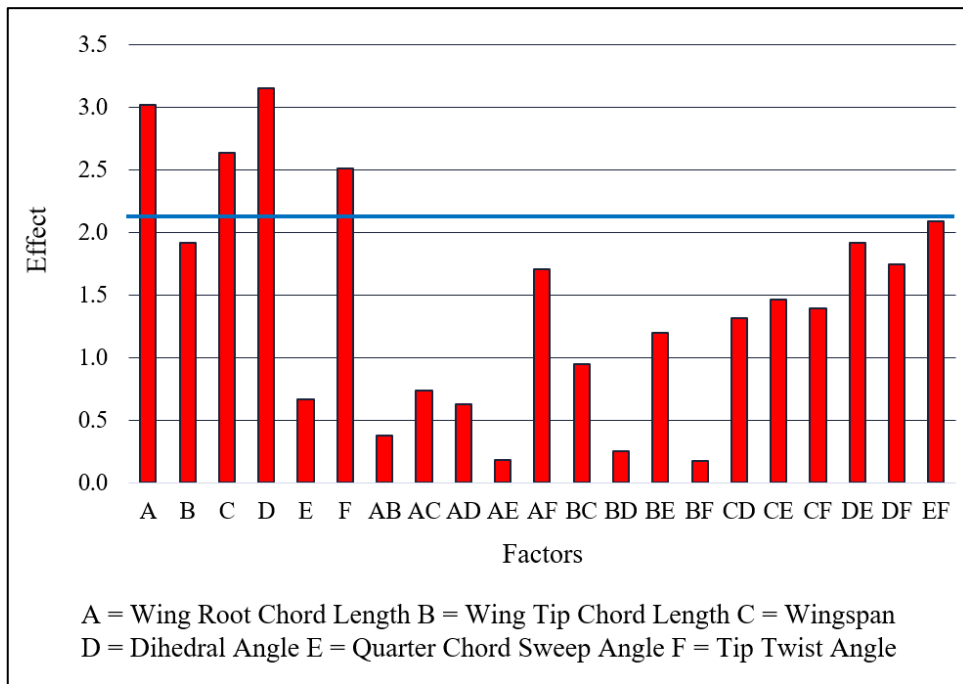


Figure 5.4 Effect of parameters on the objective function,  $C_D$ , where the blue line is drawn at the margin of error.

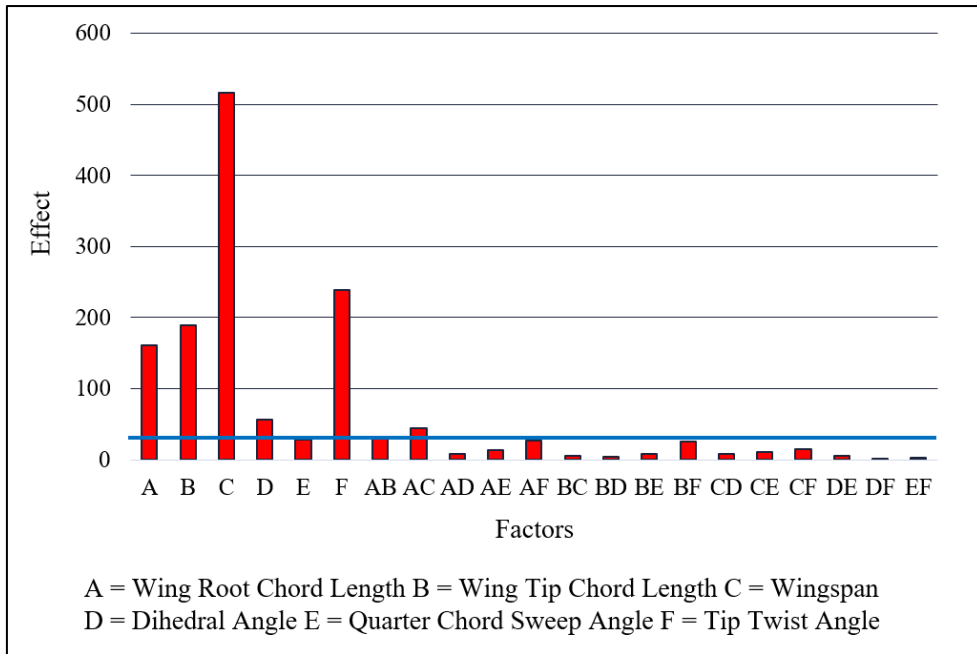


Figure 5.5 Effect of parameters on the maneuvering constraint,  $C_L$ , where the blue line is drawn at the margin of error.

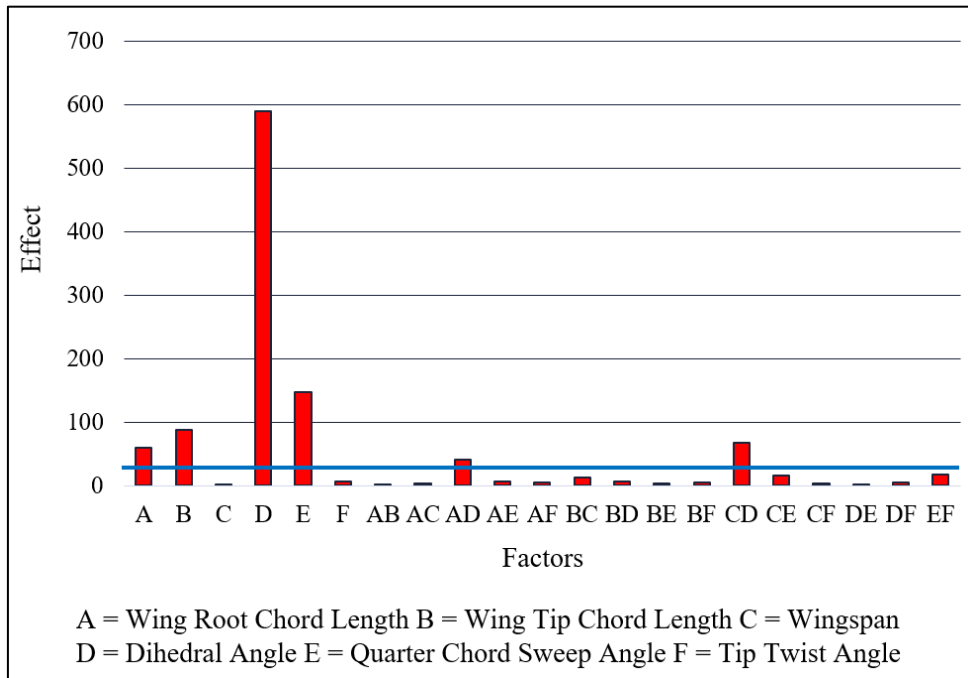


Figure 5.6 Effect of parameters on the lateral stability constraint,  $C_{RB}$ , where a blue line is drawn at the margin of error.

Figure 5.4, shows the absolute effect of main factors and two-way interactions on the value of the objective function,  $C_D$ , and a blue line is drawn at the margin of error. Values of the effect above the blue line are considered statistically significant in the figures. However, none of the interaction terms has a significant effect on the objective function as observed in Figure 5.4. Therefore, while increasing levels considering the objective function, there is no need to include design points for interaction terms.

Figure 5.5, shows the absolute effect of main factors and two-way interactions on the value of the maneuvering constraint,  $C_L$ , and the blue line is drawn at the margin of error. According to Figure 5.5, wing root chord length – wing tip chord length and wing root chord length – wingspan interactions have a significant effect on the  $C_L$ .

Figure 5.6, shows the absolute effect of main factors and two-way interactions on the value of the lateral stability constraint,  $C_{RB}$ , and the blue line is drawn at the margin of error. According to Figure 5.6, wing root chord length – dihedral angle and dihedral angle – wingspan interactions have a significant effect on the  $C_{RB}$ . As a result, levels are increased from two to four by including only statistically significant interactions.

### **5.3 Updating the Design of Experiment**

Levels are increased to four by only including interaction terms according to results obtained in Section 5.2. Four levels of the optimization variables are shown in Table 5.1.

Levels are determined by equally dividing the minimum and the maximum values that optimization variables could take. First, levels are increased for only main factors without including the interactions. This is performed by setting the levels of other optimization variables to the minimum values and increasing levels of factors one by one. As an example, to increase the levels of the main factor, wingspan, to four, two additional design points are shown in Table 5.2.

Table 5.1 Four levels of the optimization variables.

	<b>Level 1 (Minimum)</b>	<b>Level 2</b>	<b>Level 3</b>	<b>Level 4 (Maximum)</b>
Wing Span (meters)	7.38	9.01	10.63	12.26
Root Chord Length (meters)	1.85	2.09	2.33	2.57
Tip Chord Length (meters)	0.86	1.03	1.2	1.37
Dihedral Angle (degrees)	0	3.33	6.66	10
Quarter Chord Sweep Angle (degrees)	0	3.33	6.66	10
Twist Angle (degrees)	0	-1	-2	-3

Table 5.2 Additional design points to increase wingspan levels to four without including the interactions.

<b>Additional Design Point</b>	<b>Wing Span (m)</b>	<b>Root Chord Length (m)</b>	<b>Tip Chord Length (m)</b>	<b>Dihedral Angle (deg)</b>	<b>Quarter Chord Sweep Angle (deg)</b>	<b>Tip Twist Angle (deg)</b>
1	9.01	1.85	0.86	0	0	0
2	10.63	1.85	0.86	0	0	0

This process is repeated for each main factor which corresponds to additional 12 design points that are given in Appendix A. After the addition of the main factors, only statistically significant interactions are included in the factorial design. This process is performed by constructing a four-level factorial design for only statistically significant interaction terms by setting the value of the other design variables to the minimum values because they are statistically independent of the other main parameters.

This results in additional  $4^2 = 16$  design points, but eight of the design points are already included in the design space from the two-level full factorial design and the design where the main factor levels are increased. As an example of this process, Table 5.3 shows the design points to increase levels to four to include the wingspan and root chord length interaction which is statistically significant.

Table 5.3 Additional design points to include the interaction of wing span and root chord length with four levels.

<b>Marker</b>	<b>Wing Span (m)</b>	<b>Root Chord Length (m)</b>	<b>Tip Chord Length (m)</b>	<b>Dihedral Angle (deg)</b>	<b>Quarter Chord Sweep Angle (deg)</b>	<b>Tip Twist Angle (deg)</b>
A	7.38	1.85	0.86	0	0	0
B	9.01	1.85	0.86	0	0	0
B	10.63	1.85	0.86	0	0	0
A	12.26	1.85	0.86	0	0	0
B	7.38	2.09	0.86	0	0	0
C	9.01	2.09	0.86	0	0	0
C	10.63	2.09	0.86	0	0	0
C	12.26	2.09	0.86	0	0	0
B	7.38	2.33	0.86	0	0	0
C	9.01	2.33	0.86	0	0	0
C	10.63	2.33	0.86	0	0	0
C	12.26	2.33	0.86	0	0	0
A	7.38	2.57	0.86	0	0	0
C	9.01	2.57	0.86	0	0	0
C	10.63	2.57	0.86	0	0	0
A	12.26	2.57	0.86	0	0	0

In Table 5.3, marker “A” stands for design points already included in the two-level full factorial design, marker “B” stands for design points already included while increasing levels of main factors to four without interactions, and marker C stands for new design points.

As it could be observed from Table 5.3, for each statistically significant interaction term, additional eight design points are required. A similar procedure is followed for all statistically significant interactions and in total 44 additional design points are added to the two-level full factorial design. Additional design points are given in Appendix, B, C, D, E as a full table.

#### 5.4 Validation of Response Surface Models.

By using  $64 + 44 = 108$  design points and RANS solutions for each of the responses, regression models are constructed, and adjusted  $R^2$  values of the models are given in Table 5.4.

Table 5.4 Adjusted  $R^2$  values of the regression models.

<b>Response</b>	<b>Adjusted <math>R^2</math></b>
CD at 0.528 Mach Condition	98.23%
CL at 0.4 Mach Condition	99.98%
CRB at 0.186 Mach Condition	99.78%

According to Table 5.4, adjusted  $R^2$  values are above 95% which is acceptable. After regression models are constructed, RANS solutions are obtained for 11 different wings corresponding to approximately %10 of the design space with random design variables. Results of the RANS solutions are compared with the results of the regression model in the form of high-order nonlinear analytical functions. Table 5.5 shows relative errors of the regression models.

Table 5.5 Relative error percentages of regression models.

Test Design Point	Error Percentage for Regression Model of $C_D$	Error Percentage for Regression Model of $C_L$	Error Percentage for Regression Model of $C_{RB}$
1	2.59	0.06	0.56
2	0.28	0.05	0.45
3	4.43	0.01	1.70
4	3.01	0.06	0.17
5	0.69	0.24	0.31
6	2.35	0.11	1.33
7	4.67	0.33	0.39
8	0.15	0.27	0.59
9	2.87	0.37	0.05
10	4.23	0.13	1.58
11	0.10	0.09	1.07

According to Table 5.5, the error percentages are maximum %4.67 for  $C_D$ , %0.5 for  $C_L$ , and %1.7 for  $C_{RB}$ . The accuracy of the model is considered acceptable and used in the optimization. If the error percentages are obtained more than %10, the design space will be updated and models will be reconstructed.

As a result, surrogate models are constructed by obtaining 324 RANS solutions. However, to construct surrogate models with a four-level full factorial design which is a traditional approach, 12228 RANS solutions are required. Therefore the number

of RANS solutions required is decreased 97.35% compared to the traditional full factorial design by using the sequential experimentation approach.

## 5.5 Effect of the Airfoil Profile on the Optimum Solution

Since the airfoil profile of the wing root and tip define the aerodynamic shape of a trapezoidal wing to be optimized, the effect of airfoil profiles on the optimization process of this study is investigated.

There are different types of airfoil profiles classified according to their parameterization methods and geometric similarities called airfoil families. NACA airfoil family has been widely used in the wings. Most of the wing sections are NACA airfoils, have been influenced by NACA investigations, or optimized profiles based on NACA profiles [66]. In addition, it is possible to separate the effect of the camber and the thickness distribution on the optimization process by comparing NACA airfoil sections.

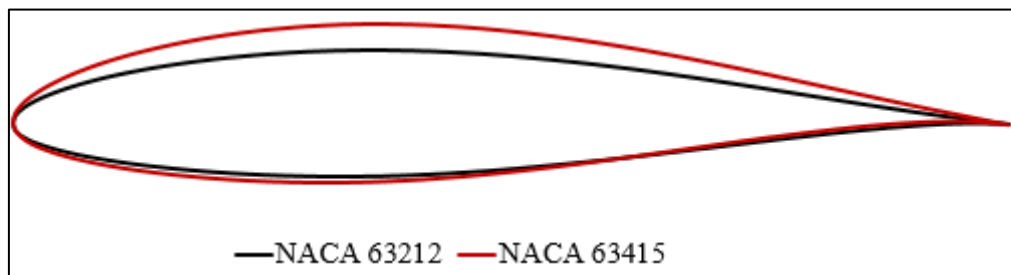


Figure 5.7 NACA 63212 and NACA 63415 airfoil profiles.

Therefore, 2-D RANS solutions are obtained by using the methodology explained in Chapter 3 for two different NACA airfoils to observe the effect of the airfoil profile on the lift and the drag coefficients. RANS solutions are obtained for NACA 63212 and NACA 63415 airfoils because two airfoils have different minimum pressure locations, design lift coefficients which could be considered as a measure of camber and maximum thicknesses [67]. In addition, 6-series are widely used in turboprop trainers. The airfoil profiles, NACA 63212 and NACA 63415, are shown in Figure 5.7.

The lift and drag coefficient vs the angle of attack are shown in Figure 5.8 and Figure 5.9 respectively for both NACA 63212 and NACA 63415 airfoils obtained from 2-D RANS solutions.

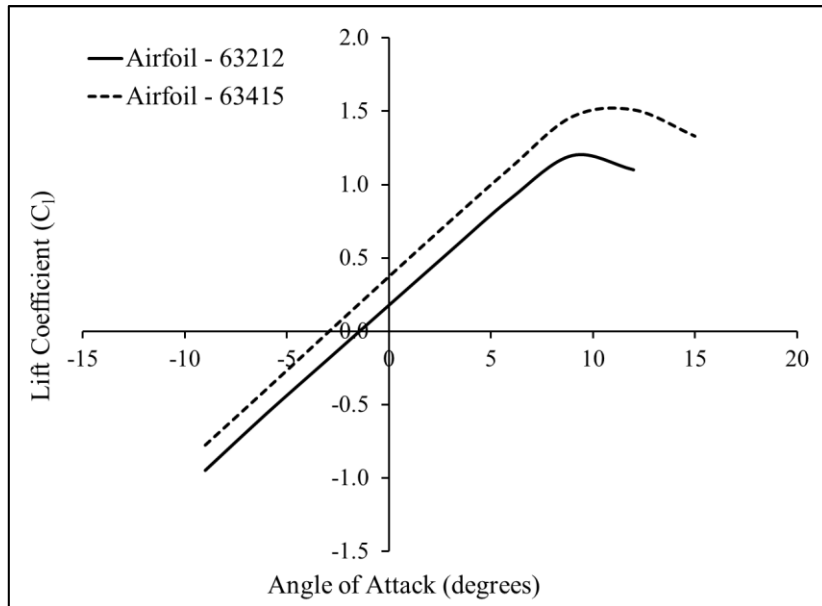


Figure 5.8 Comparison of NACA 63212 and NACA 63415 airfoils in terms of lift coefficient ( $C_l$ ).

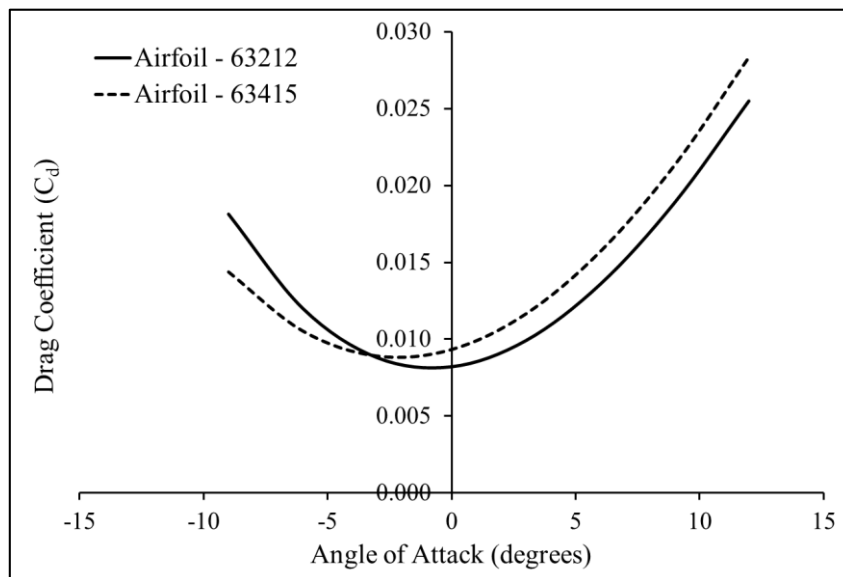


Figure 5.9 Comparison of NACA 63212 and NACA 63415 airfoils in terms of drag coefficient ( $C_d$ ).

According to Figure 5.8, the lift coefficient at each angle of attack and the maximum lift coefficient is higher for NACA 63415 airfoil compared to NACA 63212 airfoil. It is expected to achieve a higher lift coefficient and the maximum lift coefficient for NACA 63415 because the thickness increases. Besides, due to an increase in the camber, the thickness becomes more effective in terms of maximum lift coefficient for airfoils with up to 18% thickness [67]. In addition, due to the increase in the lift coefficient, the drag coefficient is higher for NACA 63415 airfoil when the lift is generated which is observed in Figure 5.9. However, the minimum drag coefficient is less for NACA 63212 airfoil due to a decrease in the camber and thickness.

After performing 2-D RANS solutions, 3-D RANS solutions are performed for two different wings with the same wingspan, root chord length, tip chord length, quarter chord sweep, tip twist, and dihedral angles, but different airfoil profiles.

To be able to associate 2-D solution results with the 3-D solution results, the same airfoil profiles NACA 63212 and NACA 63415 are used in the wings. The lift and the drag coefficient vs the angle of attack are shown in Figure 5.10 and Figure 5.11 respectively for the wings with NACA 63212 and NACA 63415 airfoils.

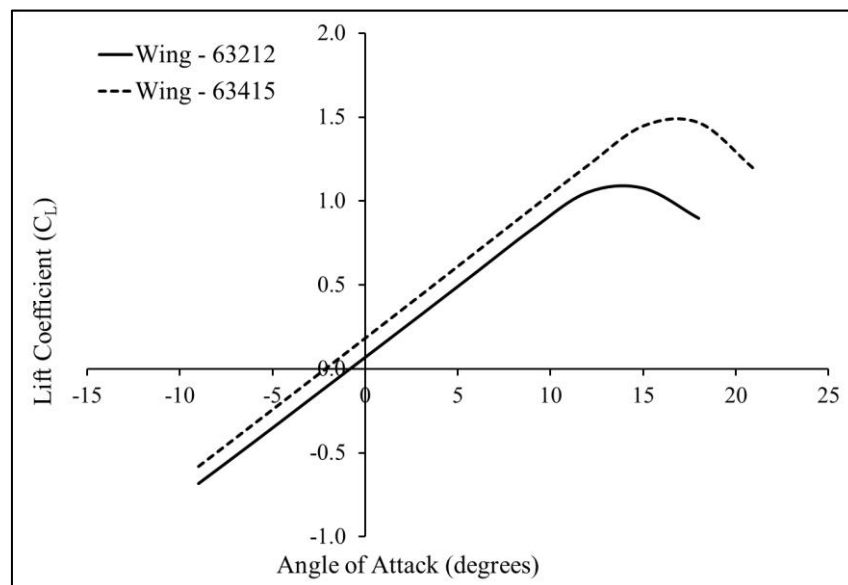


Figure 5.10 Comparison of wings with NACA 63212 and NACA 63415 airfoils in terms of lift coefficient ( $C_L$ ).

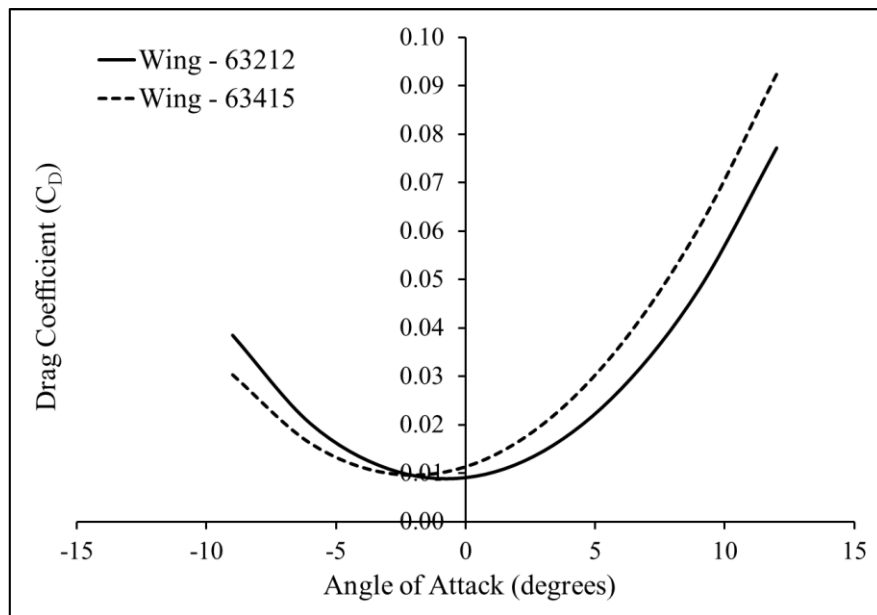


Figure 5.11 Comparison of wings with NACA 63212 and NACA 63415 airfoils in terms of drag coefficient ( $C_D$ ).

According to Figure 5.10, the lift coefficient is higher for a wing with NACA 63415 airfoil. When Figure 5.8 and Figure 5.10 are compared, it is observed that the change of the lift coefficient of two different wings with different airfoils has a similar trend with the change of the lift coefficient of two different airfoils.

Although a similar trend is observed in the figures, the magnitude of the lift coefficient difference between the two wings is different compared to the difference between two airfoils. The difference of magnitudes is due to the induced effects which depend on the aspect ratio for the lift coefficient [68].

According to Figure 5.11, the drag coefficient is higher for a wing with NACA 63415 airfoil when the lift is generated. However, the minimum drag coefficient is less for a wing with NACA 63212 airfoil due to a decrease in the thickness and the maximum camber of the profile. When Figure 5.9 and Figure 5.11 are compared, it is observed that the change of the drag coefficient of two different wings with different airfoils has a similar trend with the change of the drag coefficient of two different airfoils.

Although a similar trend is observed in the figures, the magnitude of the drag coefficient difference between the two wings is different compared to the difference between two airfoils. The difference of magnitudes is mainly due to the aspect ratio and the Oswald's efficiency of the wing for the drag coefficient [68].

Considering the comparison between 2-D and 3-D solutions, the change in the lift and drag coefficients for a wing due to its airfoil profile has a similar trend but a different magnitude compared to the change in the lift and the drag coefficients due to airfoil profiles themselves.

Since the lift and drag curves for different airfoil profiles are shifted in magnitude but their slopes are similar, it may be assumed that the airfoil profile does not have a significant influence on the planform optimization of a wing which is based on the gradient information in the design space.

To examine the effect of the airfoil profile on the optimum wing configuration two optimization studies are performed with three design variables; wingspan, root chord length, and tip chord length by using the NACA 63212 and the NACA 63415 airfoils. Validated surrogate models are used in the optimization.

The first optimization study is performed to minimize the drag coefficient while keeping the lift coefficient constant at 0.1 at  $M_\infty = 0.528$ . The variation of the design variables and the drag coefficient along the optimization steps are shown in Figure 5.12 and Figure 5.13.

As observed in Figure 5.12, in both cases the optimization variables rapidly converge the same values independent of the airfoil. However, the objective function values at the end of the optimization are different due to airfoil profiles as observed in Figure 5.13.

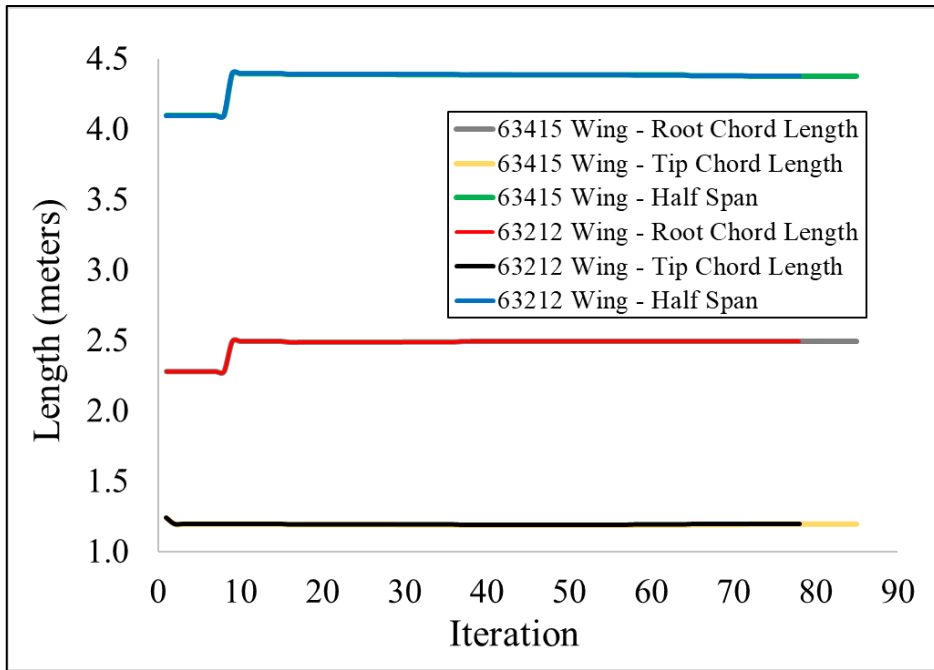


Figure 5.12 Design parameter values at each optimization iteration obtained in the first optimization study.

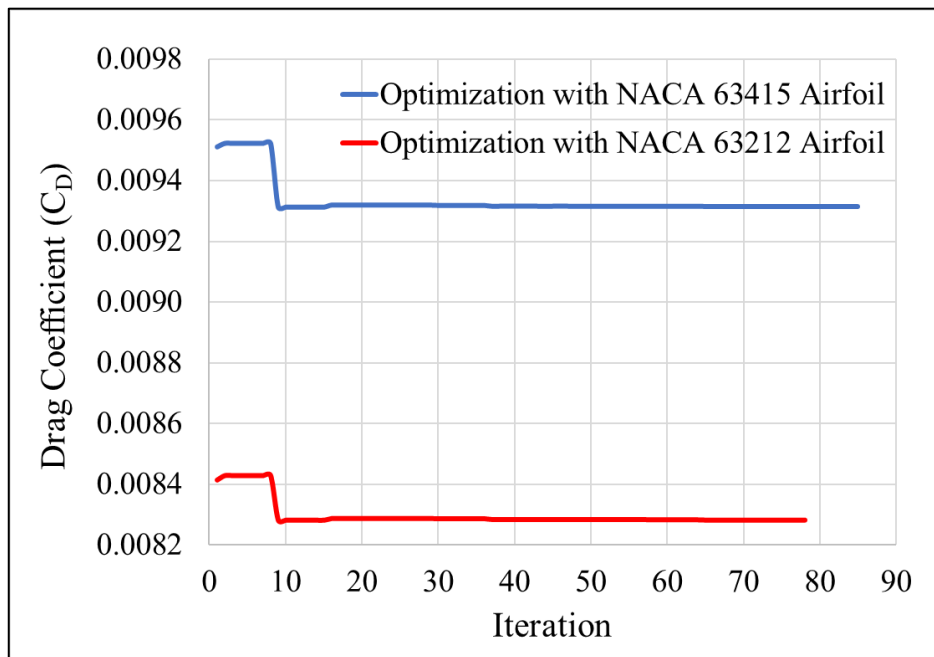


Figure 5.13 Objective function values at each optimization iteration obtained in the first optimization study.

A constrained optimization study is also performed in order to assess the profile effect. In addition to the constant lift coefficient at  $M_\infty = 0.528$ , the lift coefficient at  $M_\infty = 0.4$  and  $AoA = 10^\circ$  is constrained to be at least 1.05 to provide a desired maneuverability. The variation of the optimization variables and the drag and lift coefficients are similarly given in Figure 5.14 - Figure 5.16. As seen, the drag coefficient now increases in both cases due to the higher lift coefficient constraint, and the minimum drag coefficient is satisfied at different lift coefficient values. However, the design variables for both cases again converge to the same values (Figure 5.16).

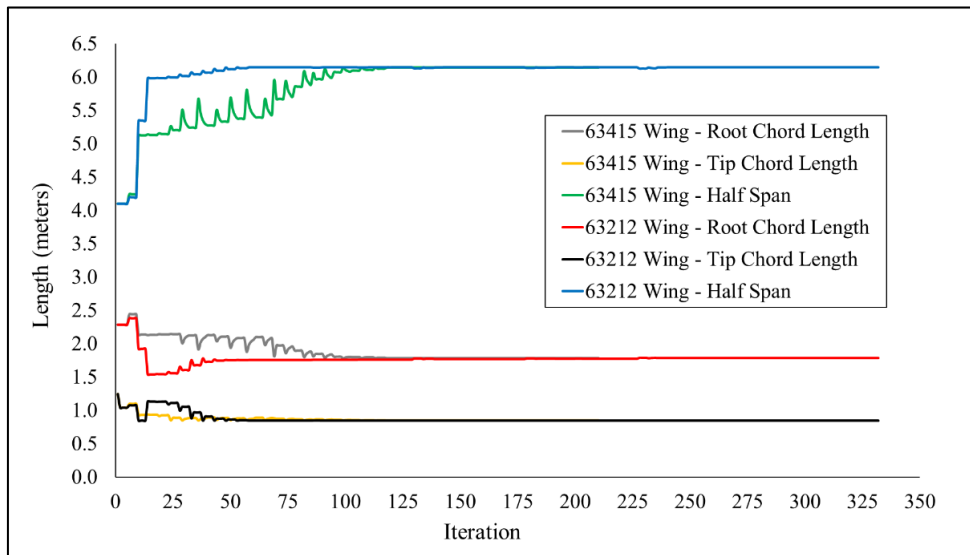


Figure 5.14 Design parameter values at each optimization iteration obtained in the second optimization study.

As it is observed in the both optimization cases, although the airfoil profiles are different, the optimum values of the design variables turned out to be the same as expected. It is concluded that if the planform optimization is performed to minimize the drag coefficient under a constant or a constrained lift coefficient, the airfoil profile does not play a significant role. Therefore, in the remaining part of the study, the airfoil profiles are not considered among the optimization variables. NACA 63415 profile is used in the root and NACA 63212 profile is used in the tip of the wing. They are widely used 6-series NACA airfoils.

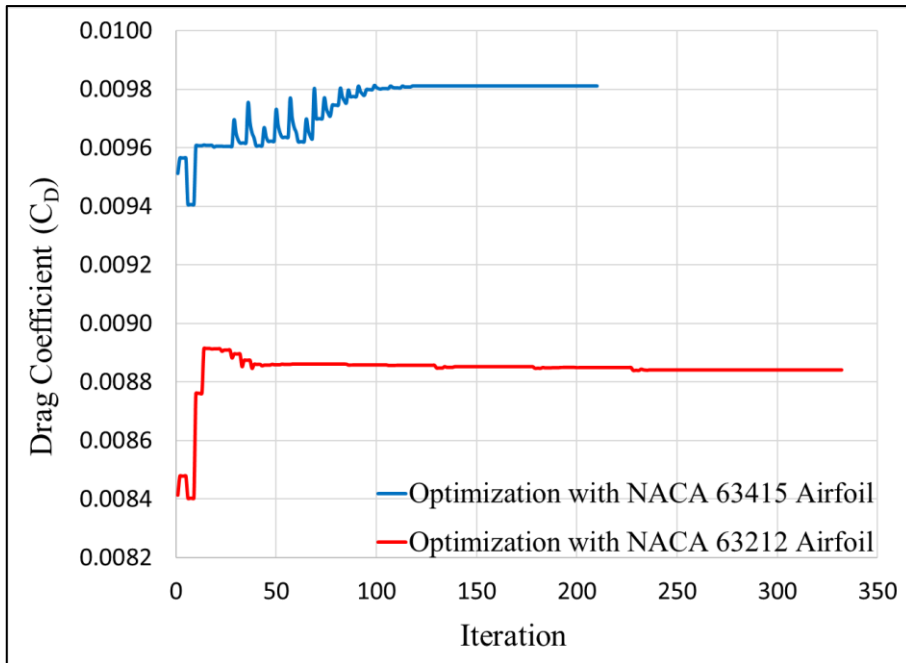


Figure 5.15 Objective function values at each optimization iteration obtained in the second optimization study.

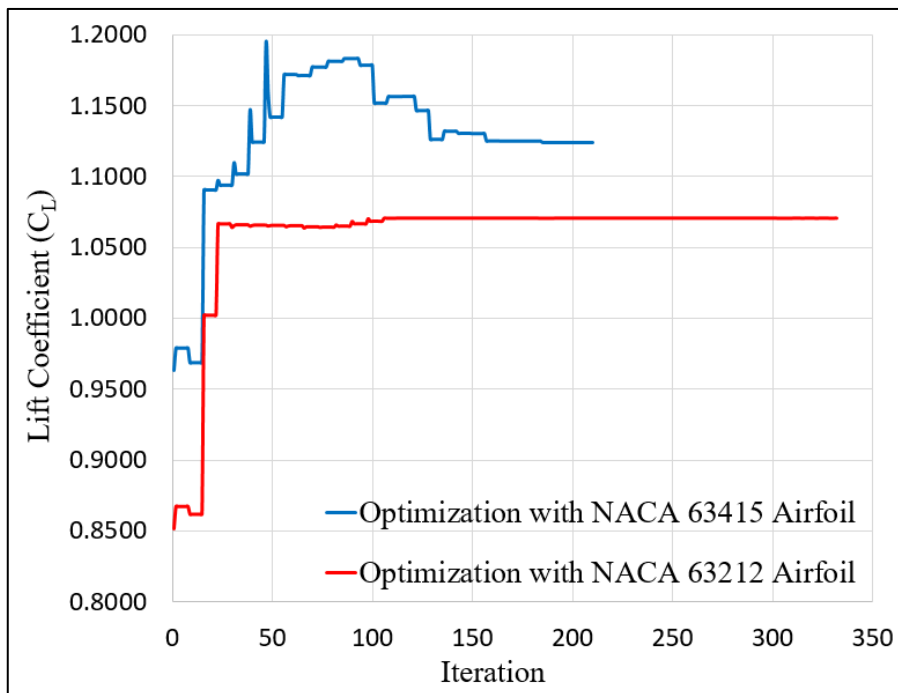


Figure 5.16 The lift coefficient value at each optimization iteration obtained in the second optimization study.

## 5.6 Optimization of the Wing Planform.

Optimization is performed by using the validated surrogate models that are nonlinear analytical functions with six design variables; wingspan, root chord length, tip chord length, quarter chord sweep angle, tip twist angle, and dihedral angle. The aim of the optimization is to minimize the drag coefficient while keeping the lift coefficient constant at 0.1.

In addition to the constant lift coefficient at  $M_\infty = 0.528$ , the lift coefficient at  $M_\infty = 0.4$  and  $AoA = 10^\circ$  is constrained to be at least 1.05 to provide a desired maneuverability. Considering the lateral stability, the rolling moment coefficient change with respect to sideslip angle at  $M_\infty = 0.186$ ,  $AoA = 8^\circ$  is constrained as well.

Additional geometric constraints are also defined in the optimization. Considering the mission profile, the reference area of the wing is set to  $16.21\text{m}^2$ . The taper ratio and the aspect ratio are constrained to take the wing weight into consideration. The taper ratio is set to be between 0.3 and 0.6, and the aspect ratio is set to be between 4 and 7.5.

The optimization is performed with two different algorithms and the variations of the objective function are shown in Figure 5.17.

According to Figure 5.17, it is observed that the sequential quadratic programming algorithm converges to the same objective function value faster than the interior point method. The interior point algorithm uses the conjugate gradient to determine the next step. However, in the sequential quadratic programming, the Hessian is used at each step which converges faster compared to the conjugate gradient step. Therefore, sequential quadratic programming is used in the remainder of the study.

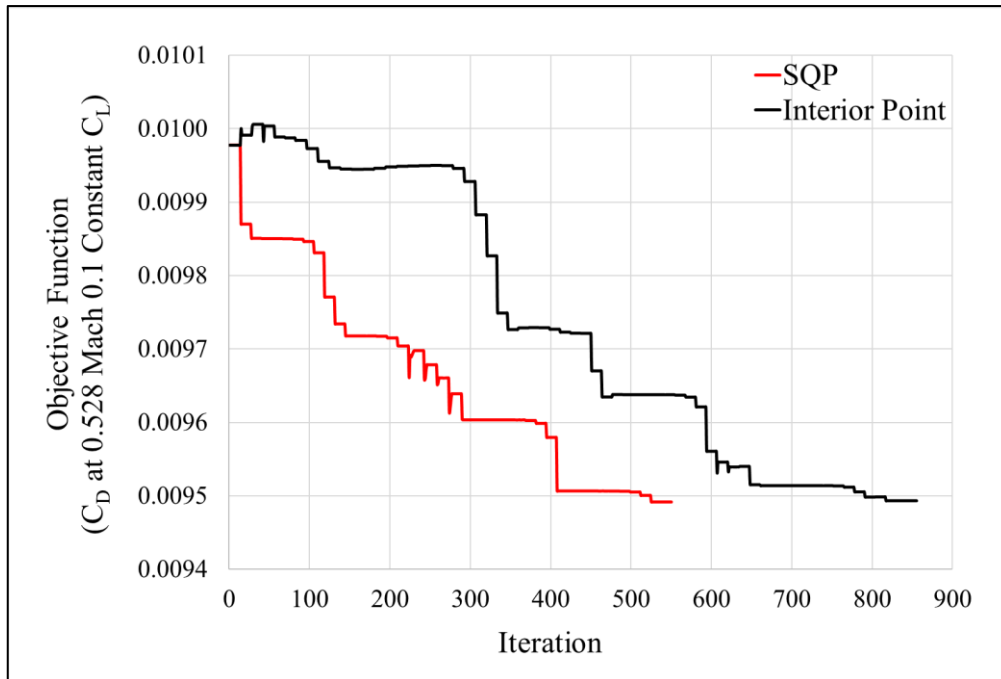


Figure 5.17 The objective function value during optimization steps.

In order to scan the design space, few more optimizations are performed with different initial conditions. The corresponding variations of the objective function are shown in Figure 5.18. Initial condition 1 is the middle point of the design space and other initial conditions are competitors PC-21, KT-1, Tucano, and Hürkuş respectively.

It is observed from Figure 5.18 that optimizations that start from initial conditions 2 and 5 converge to a much smaller value of the objective function compared to optimizations performed starting from other initial conditions. Values of the constraints are shown in Figure 5.19 and Figure 5.20 for  $C_L$  and  $C_{RB}$  values respectively for different initial conditions at each iteration step.

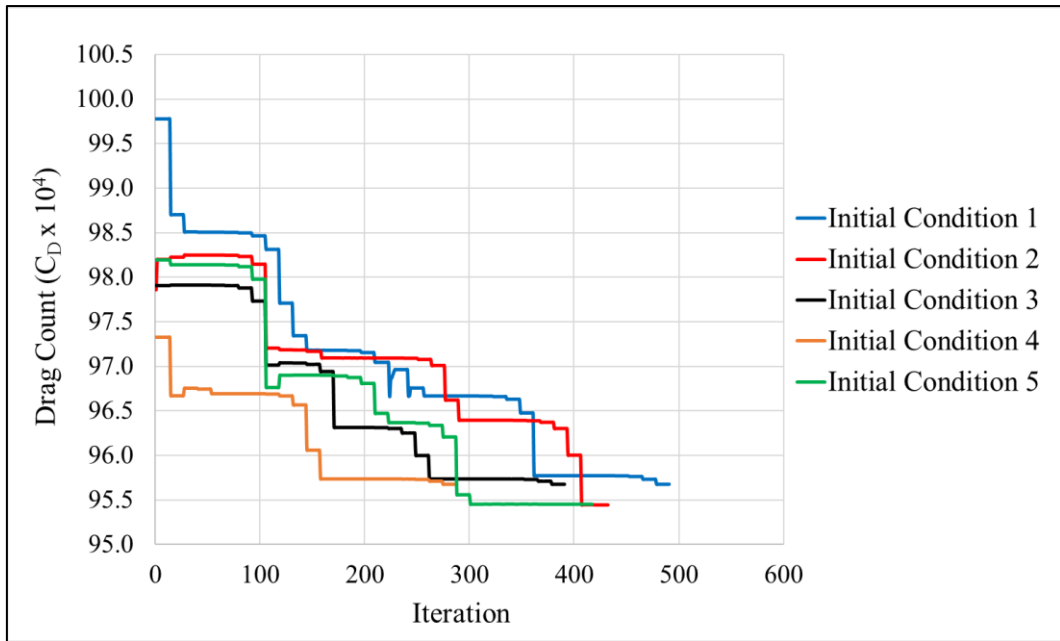


Figure 5.18 Objective function value ( $C_D$  at 0.528 Mach 0.1  $C_L$ ) at each optimization iteration.

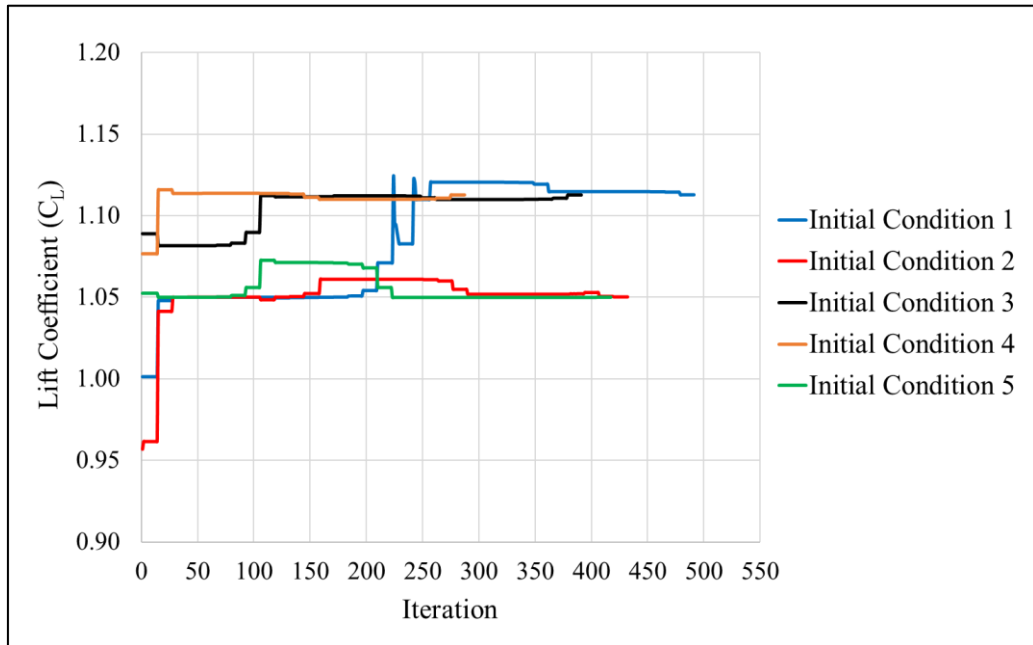


Figure 5.19 Maneuvering constraint value ( $C_L$  at 0.4 Mach) at each optimization iteration.

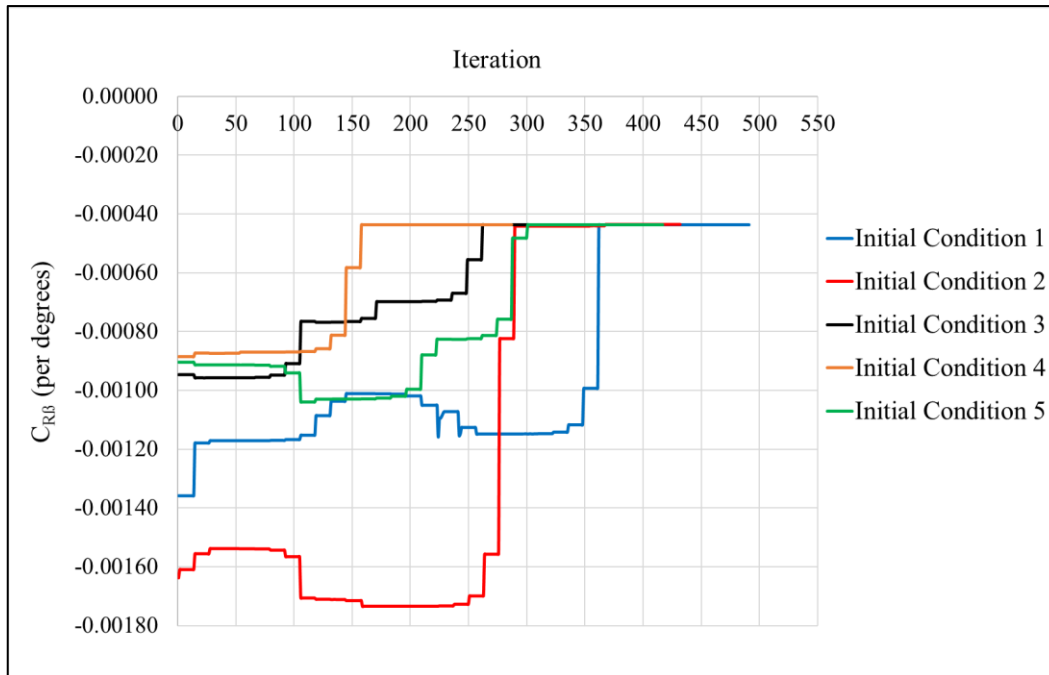


Figure 5.20 Lateral stability constraint value ( $C_{RB}$  at 0.4 Mach) at each optimization iteration.

It is observed from Figure 5.19 that all optimum configurations converge to a  $C_L$  value that satisfies the constraint. However, the 2. and 5. cases converge to a lower  $C_L$  value.

All optimum solutions converge to the same  $C_{RB}$  value which satisfies the constraint (Figure 5.20). In addition, all optimums satisfy all other constraints, the taper ratio, the aspect ratio, and the wing area.

The Table 5.6 shows the value of the objective function, the optimum values of the design variables together with their allowed limits for each case. As seen, Cases 1,3 and 4, and Cases 2 and 5 converge to the same optimum configurations. Having a smaller drag count, Case 5 (2) is taken as the optimum configuration.

Table 5.6 Optimum values of the design variables for optimizations with different initial conditions

	Case				
	1	2	3	4	5
Drag Count ( $C_D \times 10^4$ )	95.76	95.32	95.76	95.76	<b>95.32</b>
<b>Design Variable</b>					
Wingspan (m) (7.38 - 12.26)	11.026	10.131	11.026	11.026	<b>10.131</b>
Root Chord Length (m) (1.85 - 2.57)	2.09	2.00	2.09	2.09	<b>2.00</b>
Tip Chord Length (m) (0.86 - 1.37)	0.85	1.20	0.85	0.85	<b>1.20</b>
Dihedral Angle (deg) (0 - 10)	2.75	2.23	2.75	2.75	<b>2.23</b>
Quarter Chord Sweep Angle (deg) (0 - 10)	2.14	0.15	2.14	2.14	<b>0.15</b>
Twist Angle (deg) (-3 - 0)	0	0	0	0	<b>0</b>
<b>Constraints</b>					
Wing Area ( $m^2$ ) = 16.21	16.21	16.21	16.21	16.21	<b>16.21</b>
Taper Ratio (0.3 - 0.6)	0.41	0.6	0.41	0.41	<b>0.6</b>
Aspect Ratio (4 - 7.5)	7.5	6.33	7.5	7.5	<b>6.33</b>

The variation of the wing planform for Case 5 along the optimization steps is shown in Figure 5.21. The top and side views of the optimum wing planform are also shown in Figure 5.22.

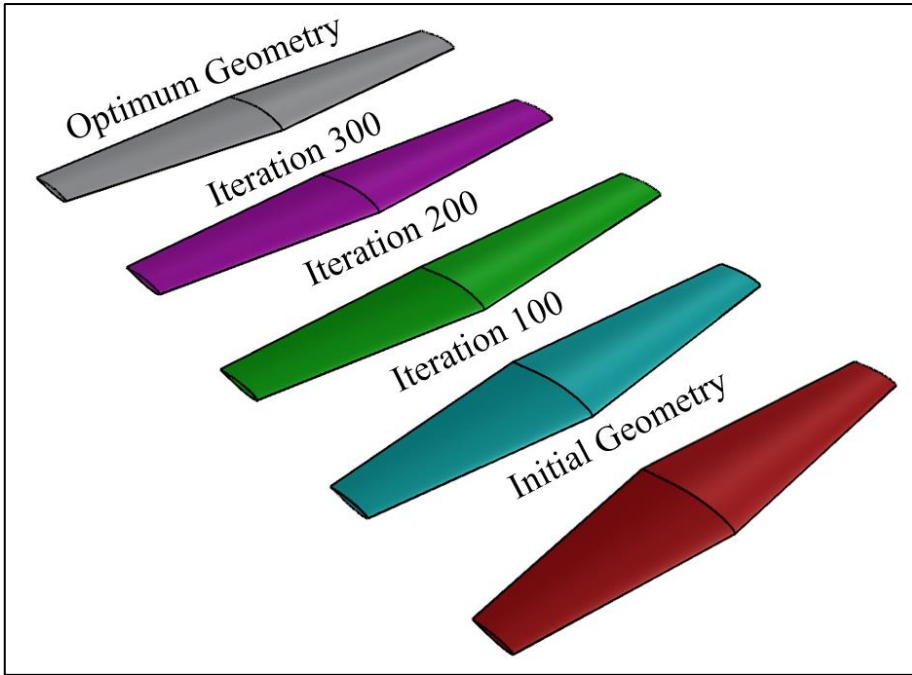


Figure 5.21 Wing configurations at different optimization steps.

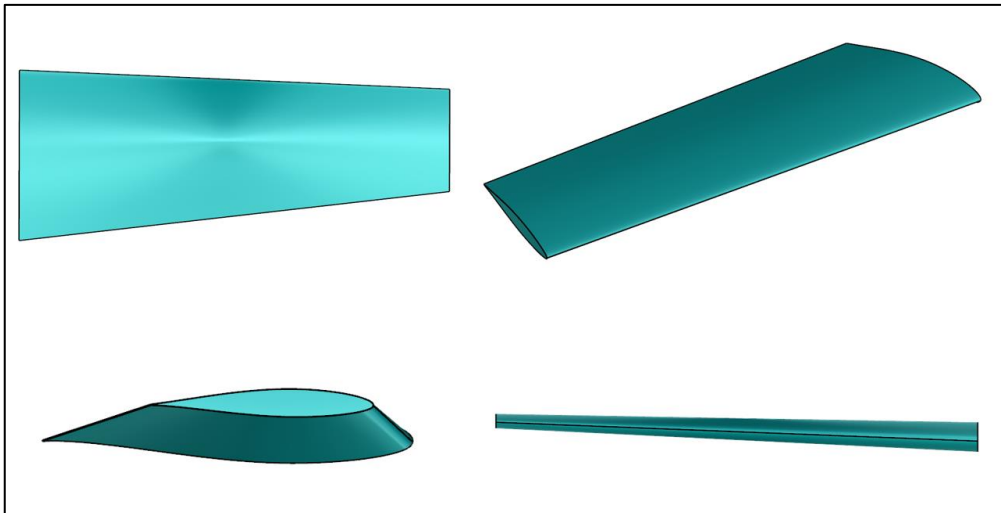


Figure 5.22 The optimum wing geometry from different views.

## 5.7 Validation of the Optimum Configuration

For the validation, the RANS solutions for the optimum configuration is performed and the drag polar at  $M_\infty = 0.528$  is compared against the initial configuration in Figure 5.23. As seen, the drag coefficient at  $C_L=0.1$  is improved by 2.93% and it is similarly improved in all the  $C_L$  range.

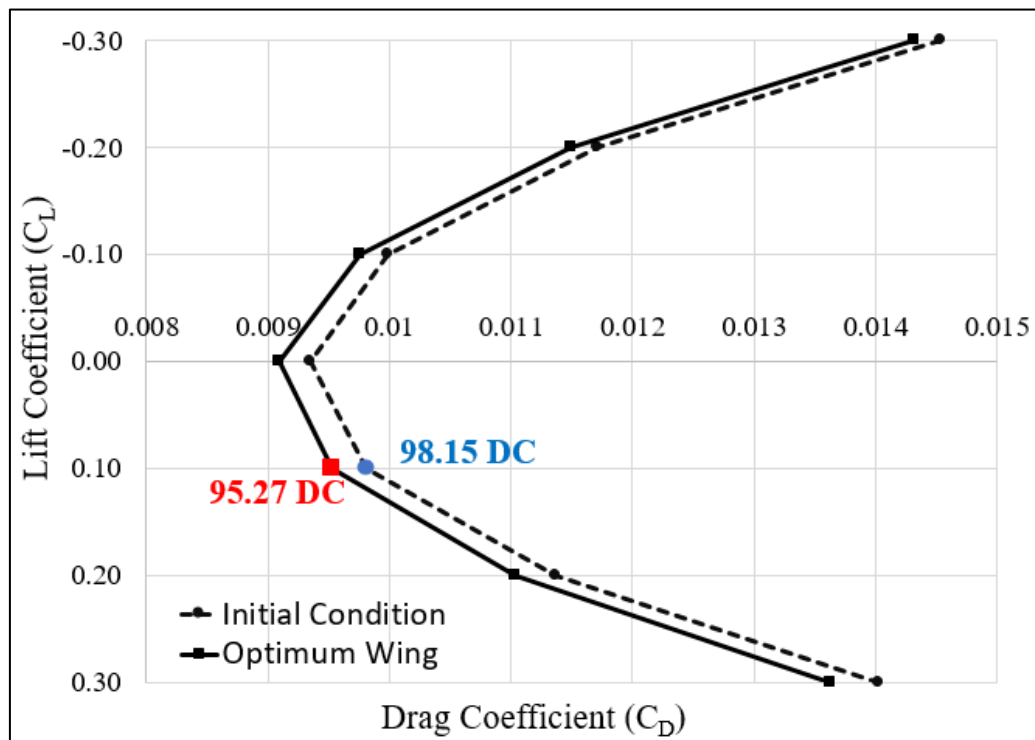


Figure 5.23 The drag polar at  $M_\infty = 0.528$  for the initial and the optimum wings.

The surface pressure coefficient distributions for the initial and the optimum wings are also shown in Figure 5.24

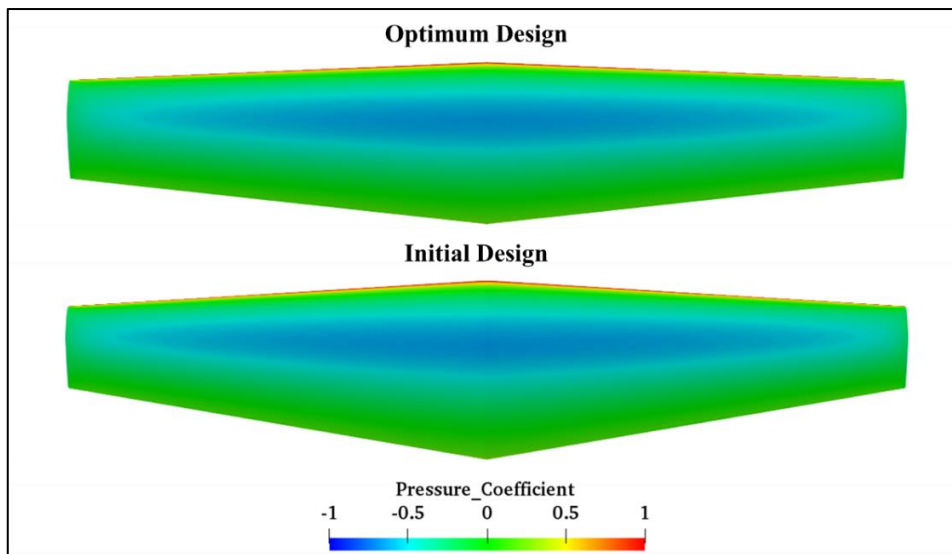


Figure 5.24 The surface pressure coefficient distributions for initial and optimum wings at  $M_\infty = 0.528$  from the top view.

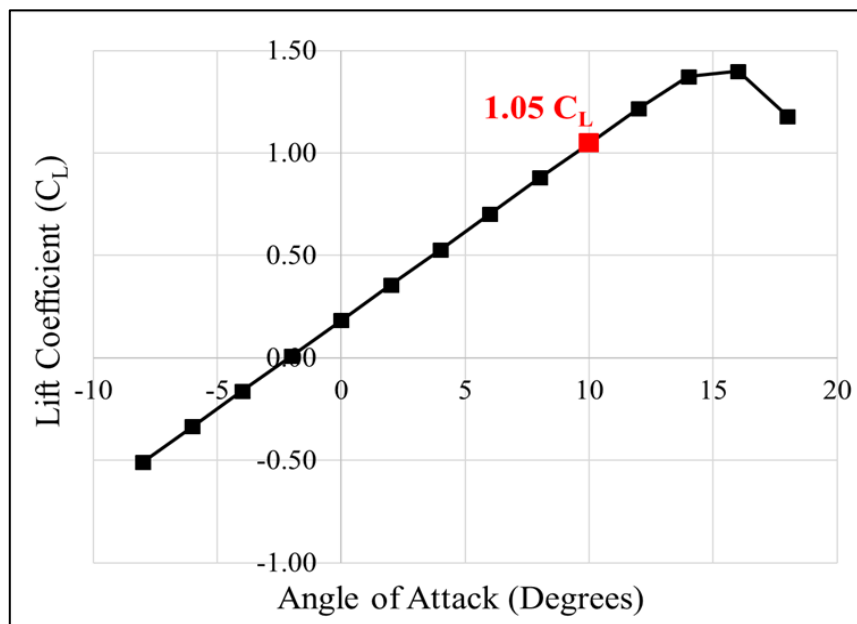


Figure 5.25 The lift coefficient ( $C_L$ ) vs angle of attack at  $M_\infty = 0.4$ .

Figure 5.25, shows the lift coefficient vs the angle of attack at  $M_\infty = 0.4$ . The optimization constraint on the lift coefficient at  $\text{AoA} = 10^\circ$ , which is marked red, is again satisfied based on the RANS solution for the optimum configuration.

In addition, the lateral stability constraint imposed on the rolling moment coefficient at  $M_\infty = 0.186$  is similarly satisfied (Figure 5.26).

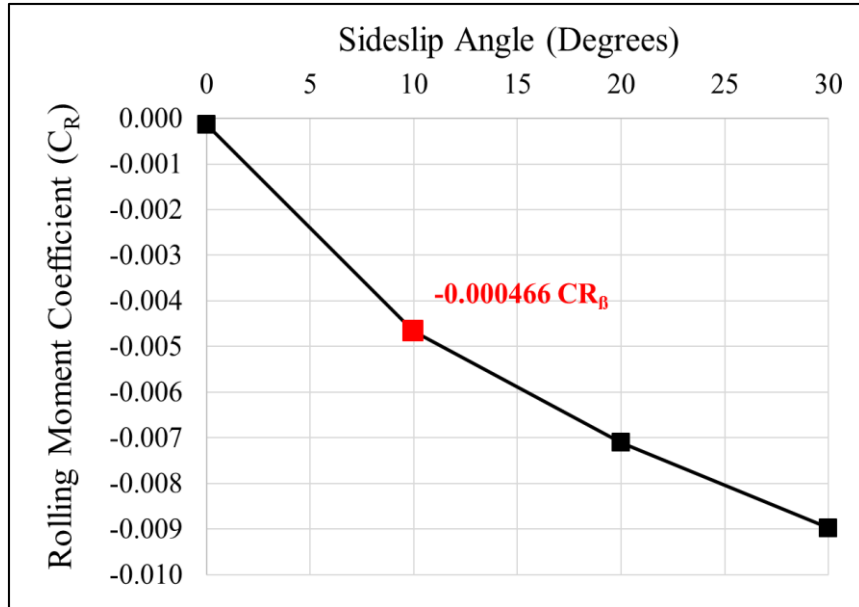


Figure 5.26 The rolling moment coefficient ( $C_R$ ) at different sideslip angles at  $M_\infty = 0.186$

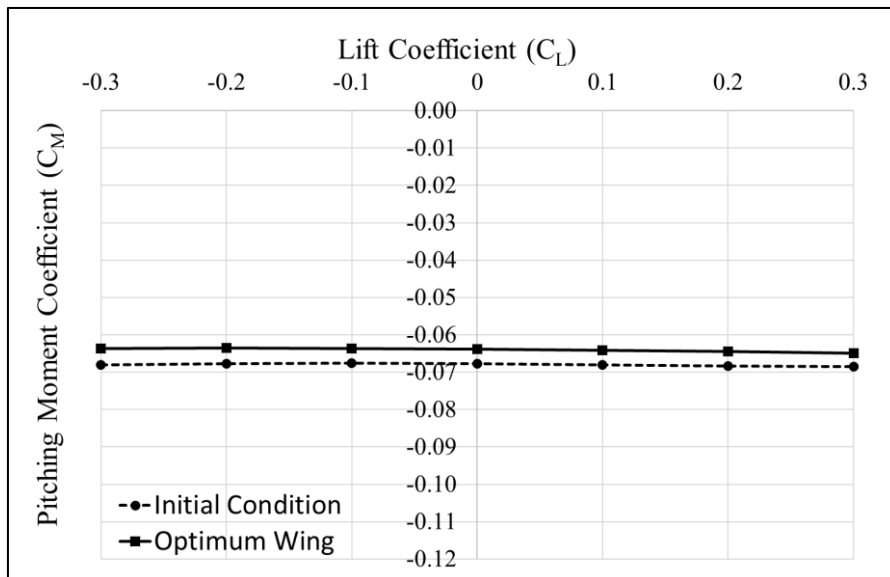


Figure 5.27 The pitching moment coefficient change vs the lift coefficient for the initial and the optimum wings.

The variation of the pitching moment coefficient vs the lift coefficient is shown in Figure 5.27 for the baseline and the optimum wing. The pitching moment coefficient is evaluated at the quarter chord of the mean aerodynamic chord and is close to the aerodynamic center of the wing. Even though the pitching moment is not constrained in the optimization process, it stays almost constant similar to the baseline configuration and provides similar longitudinal stability characteristics as expected. In addition, since the magnitude of the pitching moment is smaller for the optimized wing, the trim drag is improved and the moment arm of the horizontal tail area is reduced for the same level of longitudinal stability.

The initial and optimum wing planforms are compared in Figure 5.28. It is observed that the optimum planform has a larger wingspan and tip chord length, and smaller root chord length, tip twist, dihedral, and quarter chord sweep angles.

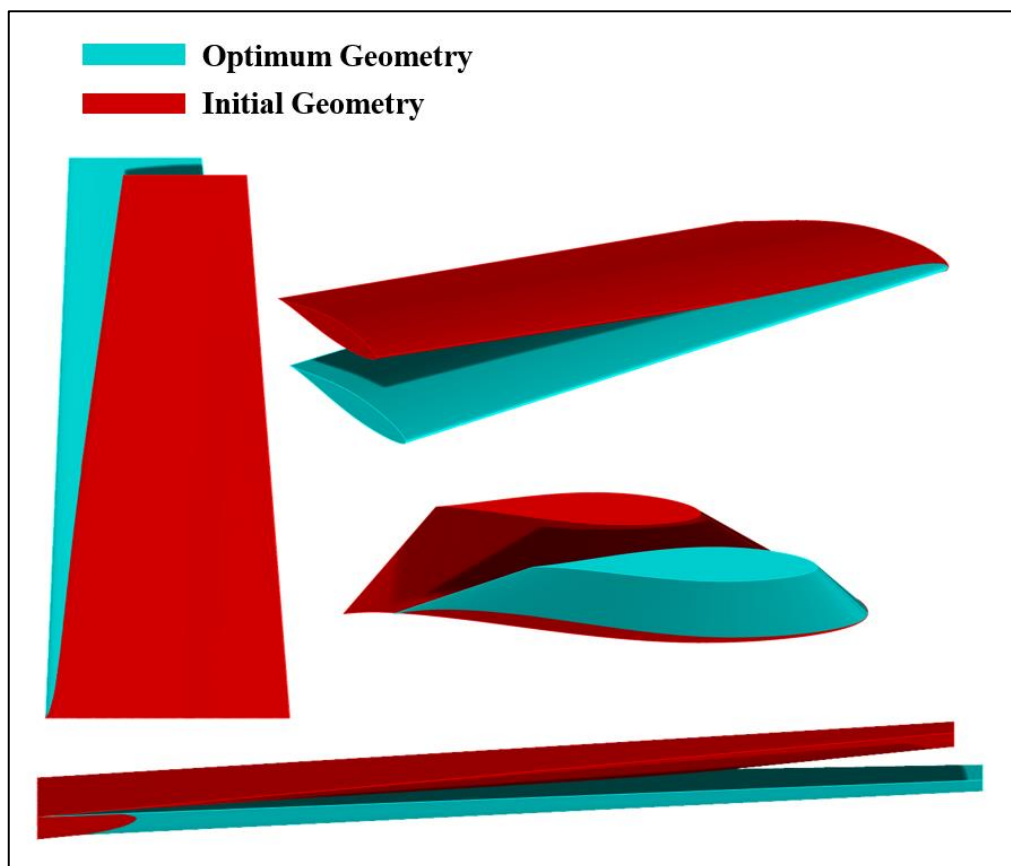


Figure 5.28 The initial and the optimum wings.

Finally, Figure 5.29 shows the optimum wing designed (Case 5) attached to the EMB 312 turboprop trainer aircraft for a visual display [69].

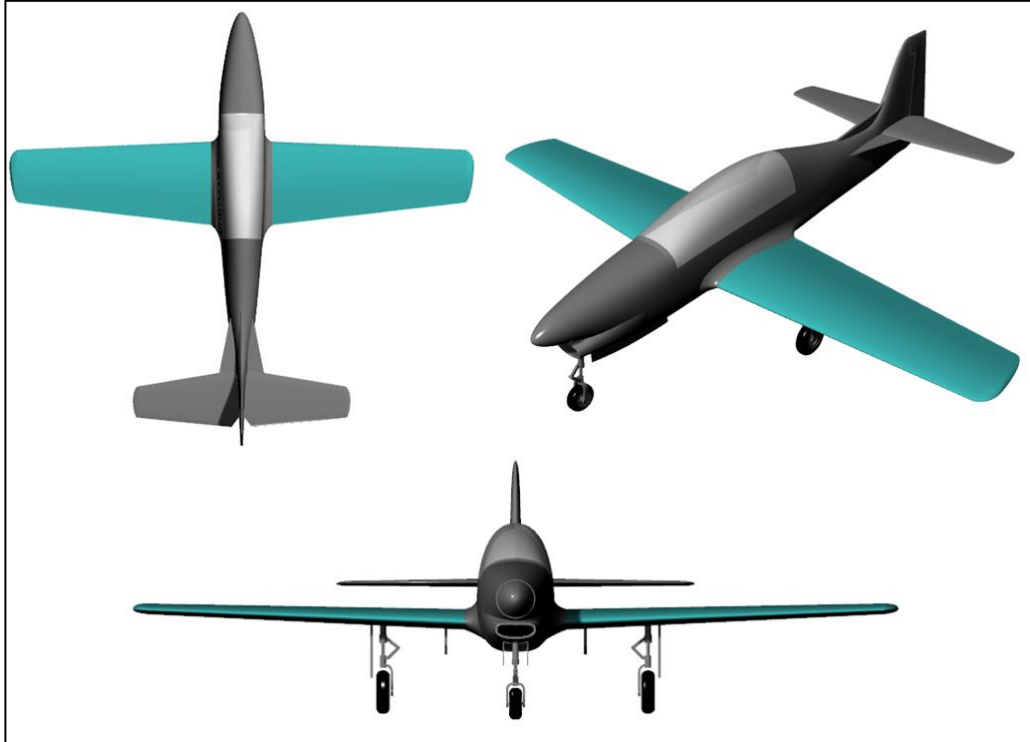


Figure 5.29 The optimized wing attached to the turboprop trainer aircraft EMB 312 body.



## CHAPTER 6

### CONCLUDING REMARKS

In this study, the aerodynamic shape of a wing for a turboprop trainer is successfully optimized by using 3D RANS solutions with SU2 and response surface methodology. A trapezoidal wing is employed and the optimization parameters are determined accordingly. The objective function and constraints are determined according to the mission requirements and the dimensions of turboprop trainer aircraft already operating.

The objective function is taken as minimizing the drag coefficient at  $M_\infty = 0.528$  while keeping the lift coefficient constant at 0.1. The fixed lift coefficient is achieved by means of RANS solutions with SU2, which provide the aerodynamic coefficients to be used in forming the response surface. In addition to the constant lift coefficient at  $M_\infty = 0.528$ , the lift coefficient is also constrained to be at least 1.05 at  $M_\infty = 0.4$  and  $AoA = 10^\circ$  to achieve the desired maneuverability. The variation of the rolling moment coefficient with respect to the sideslip angle at  $M_\infty = 0.186$ ,  $AoA = 8^\circ$  is also constrained for the lateral stability. The reference area of the wing is set to  $16.21 \text{ m}^2$  to achieve the required wing loading according to the mission profile. Finally, the aspect ratio is limited between 4 and 7.5, and the taper ratio is limited between 0.3 and 0.6 to prevent a possible increase in the wing weight.

The design of experiment technique, sequential experimentation, is used to construct the surrogate models. A two-level full factorial design is first constructed to observe the effect of main factors and interactions on the response. Statistically significant interaction terms are determined by comparing the effect of each interaction term with the margin of error. Additional design points are then included for the design variables with the significant interaction.

As a result of the significant interaction analysis, instead of 4096 design points that are required for a four-level full factorial traditional design of experiment, 144 design points are used to create surrogate models, which reduces the number of RANS solutions by about 95%. In the RANS solutions performed for validation of the surrogate model, the maximum relative error is found to be 4.67% for  $C_D$ , 0.5% for  $C_L$ , and 1.7% for  $C_{RB}$ .

The effect of the airfoil profile on the shape optimization of the wing is assessed by performing unconstrained and constrained optimizations with two different airfoil profiles, NACA 63212 and NACA 63415. Surrogate models are constructed for three optimization variables; wingspan, root chord length, and tip chord length. The optimum solutions for the minimum drag at the constant lift coefficient produced the same wing planforms for both airfoils. It is attributed to the fact that the surrogate models are formed with the constant lift coefficient SU2 solutions, and in the remainder of the study NACA 63415 and NACA 63212 profiles are employed at the wing root and at the tip, respectively.

Finally, the optimization studies with various initial conditions and optimization algorithms are performed with the optimization variables; wingspan, root chord length, tip chord length, quarter chord sweep angle, tip twist angle, and dihedral angle. It is observed that all the optimization algorithms converge to the same solution but the sequential quadratic programming provides the optimum solutions faster.

The constrained optimizations performed with five different initial conditions provided two local optimum solutions, one with a smaller drag coefficient, which is taken as the optimum configuration. The optimum configuration decreases the drag coefficient by 2.93% at  $M_\infty = 0.528$ . In conclusion, the aerodynamic shape optimization of a wing to minimize the drag coefficient at a constant lift coefficient is performed successfully by using 3D RANS solutions and the response surface methodology.

As a future work, the presented methodology may be employed for the shape optimization of the horizontal tail together with the wing. Following the planform optimization, the profile optimization of the wing may further be performed. Due to the large number of design variables involved in defining an airfoil profile, adjoint based algorithms may be used more efficiently.



## REFERENCES

- [1] NASA, “Parts of an Airplane”, Grades 9-12, Aeronautics Research Mission Directorate, 2010.
- [2] Saarlans M., “Aircraft Performance”, John Wiley & Sons, Inc., 2007.
- [3] Filippone A., “Flight Performance of Fixed and Rotary Wing Aircraft”, Elsevier, 2006.
- [4] Swatton P. J., “Aircraft Performance Theory for Pilots”, Blackwell Science, 2005.
- [5] Masefield O. L. P., “Design of a Manual Roll Control for a Trainer Aircraft”, *Phd Thesis*, Loughborough University, 1995.
- [6] Frased, D. C., “Flying Qualities”, *Journal of Guidance, Control and Dynamics*. 9 (5), doi:10.2514/3.56420
- [7] Tewari, A. “Basic Flight Mechanics A Simple Approach Without Equations”, Springer, 2016.
- [8] Kermode A.C., “Mechanics of Flight”, Revised by Barnard R. H., Philpott D. R., Pearson, 2006.
- [9] Hull D. G., “Fundamentals of Airplane Flight Mechanics”, Springer, 2007.
- [10] Turkish Aerospace (TUSAS) website : [www.tusas.com](http://www.tusas.com). Last accessed 14.02.2021.
- [11] Turkish Air Forces, General Information About Flight Training, <https://www.hvkk.tsk.tr/Custom/Hvkk/131>. Last accessed 14.02.2021
- [12] United States Air Forces (USAF), “Flying Training”, <https://www.aetc.af.mil/Flying-Training/> Last accessed 14.02.2021.
- [13] Swiss Armed Forces, PC-21 Jet Pilot Training System, <https://www.vtg.admin.ch/en/einsatzmittel/luft/pc-21.html>. Last accessed, 14.02.2021

- [14] Tomahawk Aviation USA website: <https://tomahawk-aviation-usa.com/pilatus-pc-21-turbopro>. Last accessed 14.02.2021
- [15] Pilatus, “PC-21 Brochure”, <https://www.pilatus-aircraft.com/data/document/Pilatus-Aircraft-Ltd-PC-21-Brochure.pdf>. Last accessed 14.02.2021.
- [16] Heiser W. H., Mattingly J. D., “Supercruise Aircraft Range”, *Journal of Aircraft Vol. 47*, 2010.
- [17] Vinh N. X., Tzeng Y. F., “Optimum Poststall Turning and Supersonic Turning”, *AIAA Flight Simulation and Technologies*, 1993.
- [18] Peigin S., Epstein B., “3D Optimization of Aerodynamic Wings Based on Accurate CFD Computations”, *43<sup>rd</sup> AIAA Aerospace Science Meeting and Exhibit*, Nevada, 2005.
- [19] Dumont A., Méheut M., “Gradient-Based Optimization of CRM wing-alone and wing-body-tail configurations by RANS Adjoint Technique”, *AIAA Scitech 2016*, California, 2016.
- [20] Wang K., Han Z.-H., Song W.-P., Wang H., and Wu M.-M., “Aerodynamic Shape Optimization of Wing-Body-Tail Configuration via Efficient Surrogate-Based Optimization”, *AIAA Aviation Forum, Multidisciplinary Analysis and Optimization Conference*, Atlanta, 2018.
- [21] Russel, J. B., “Performance & Stability of Aircraft, Butterworth Heinemann, 1996.
- [22] Raymer, D. P., “Aircraft Design: A Conceptual Approach”, AIAA Education Series, 2019.
- [23] Kundu, A.K., Price M. A., and Riordan D., “Conceptual Aircraft Design An Industrial Approach”, Wiley, pp. 128-153, 2019.
- [24] “Jane’s All the Worlds Aircraft 2007-2008” edited by Paul Jackson, Jane’s Information Group, 2007.

- [25] “The USAF Stability and Control Digital DATCOM”, Vol. 1, Users Manual, McDonnell Douglas Astronautics Company, 1978.
- [26] Gudmundsson S., “General Aviation Aircraft Design Applied Methods and Procedures”, Butterworth-Heinemann, 2013.
- [27] Pilatus, “PC-21 Facts Sheet”, [www.pilatus-aircraft.com/data/document/Pilatus-Aircraft-Ltd-PC-21-Factsheet.pdf](http://www.pilatus-aircraft.com/data/document/Pilatus-Aircraft-Ltd-PC-21-Factsheet.pdf), Last accessed 30 January 2021.
- [28] Embraer, “Super Tucano Brochure”, <https://defense.embraer.com/global/en/super-tucano>, Last accessed 30 January 2021.
- [29] “Jane’s All the Worlds Aircraft 2004-2005” edited by Paul Jackson, Jane’s Information Group, 2004.
- [30] Tusas, “Hurkus TUSAS Information”, [www.tusas.com/urun/hurkus](http://www.tusas.com/urun/hurkus), Last accessed 27 January 2021.
- [31] Hurkus blueprints, [https://www.the-blueprints.com/blueprints/modernplanes/modern-t/81464/view/tai\\_hurkus/](https://www.the-blueprints.com/blueprints/modernplanes/modern-t/81464/view/tai_hurkus/), Last accessed 27 January 2021.
- [32] Rhinoceros, Computer Aided Design Software, ver. 5.
- [33] Garcia M. J., Boulanger P., and Giraldo S., “CFD Based Wing Shape Optimization Through Gradient-Based Method”, *International Conference on Engineering Optimization*, June 2008.
- [34] Soto O., Lohner R., and Yang C., “An Adjoint-Based Design Methodology for CFD Optimization”, *Journal of Numerical Methods for Heat and Fluid Flow*, September 2004.
- [35] Rios L. M., Sahinidis N. V., “Derivative-free Optimization: A Review of Algorithms and Comparison of Software Implementations”, *Journal of Global Optimization*, November 2009.

- [36] Lagarias J. C., Poonen B., and Wright M. H., “Convergence of the Restricted Nelder-Mead Algorithm in Two Dimensions”, *SIAM Journal on Optimization*, 2012.
- [37] Dai S., Xu B., Luo G., and Xue Z., “Applications of Design of Experiment and Desing-Space (DOE-DS) Methodology for the HPLC Separation of Panax Notoginseng Saponins”, *The Open Chemical Journal*, June 2015.
- [38] Box G. E., Hunter J. S., and Hunter W. G., “Statics for Experimenters Design, Inovation, and Discovery” Wiley, 2005.
- [39] Myers R. H., Montgomery D. C., and Anderson-Cook C. M., “Response Surface Methodology: Process and Product Optimization Using Designed Experiments”, Wiley, 2016.
- [40] Moore D. S., Notz W. I., and Flinger M. A., “The Basic Practice of Statistics”, Macmillian Learning, 2012.
- [41] EASA, “Easy Access Rules for Normal, Utility, Aerobatic, and Commuter Category Aeroplanes (CS-23)”, <https://www.easa.europa.eu/sites/default/files/dfu/CS-23%20Amendment%201.pdf>, Last accessed 31 January 2021.
- [42] Gallagher G. L., Higgins L. B., Khinoo L. A, and Pierce P. W., “U.S. Naval Test Pilot School Flight Test Manual: Fixed Wing Performance”, USNTPS-FTM-NO.108, Veda Incorporated, 1992.
- [43] Anderson J. D., “Aircraft Performance and Design”, McGraw Hill, 1999.
- [44] Ojha S. K., “Flight Performance of Aircraft”, AIAA Education Series, 1995.
- [45] Federation of American Scientists, “Multi Command Handbook 11-F16 Volume 5”, p.245, <https://fas.org/man/dod-101/sys/ac/docs/16v5.pdf>, Last accessed 31 January 2021.

- [46] *PC-21*                      *Type*                      *Certification*                      *Document*,  
www.bazl.admin.ch/dam/bazl/de/dokumente/Fachleute/Luftfahrzeuge/  
TCDS/foca-f-56-35-6.pdf.download.pdf/foca-f-56-35-8.pdf, Last accessed  
31 January 2021.
- [47] Raymer, D. P., “Aircraft Design: A Conceptual Approach”, AIAA  
Education Series, p. 510, 2019
- [48] Wright-Patterson AFB, “Military Specification”, *MIL-F-8785C*, 5  
November 1980.
- [49] MathWorks, Matlab, *Computer Software*, ver. 2017.
- [50] MathWorks, “*Matlab Help Center*”, <https://www.mathworks.com/help/>,  
Last accessed 31 January 2021.
- [51] Nocedal J., Wright S. J., “Numerical Optimization”, Springer, 1999.
- [52] Stanford, *SU2, An Opensource CFD Software*, ver. 6
- [53] Economon T. D., Palacios F., Aranke A. C., Copeland S. R., Lonkar K. A.,  
Lukaczyk T. W., Manosalvas D. E., Naik K. R., Padron A. S., Tracey B.,  
Variyar A., and Alonso J. J., “Stanford University Unstructured (SU<sup>2</sup>):  
Open-source Analysis and Design Technology for Turbulent Flows, AIAA  
Scitech, 2014.
- [54] Economon T. D., Palacios F., Copelan S. R., Lukaczyk T. W., and Alonso  
J. J., “SU2: Open-Source Suite for Multiphysics Simulation and Design
- [55] Jameson A., “Analysis and Design of Numerical Schemes for Gas  
Dynamics 2 Artificial Diffusion, and Discrete Shock Structure”,  
*International Journal of Computational Fluid Dynamics*, September 1994.
- [56] Wen-long W., Hua L., and Sha P., “Performance Comparison and Analysis  
of Different Schemes, and Limiters”, *International Journal of Physical and  
Mathematical Sciences*, Vol:5, No:7, 2011.

- [57] Tong O., “Verification and Validation of the Spalart-Allmaras Turbulence Model for Strand Grids. *MS Thesis*, Utah State University, 2013.
- [58] Schulze D., “Far-Field Boundary Conditions Based on Characteristic and Bicharacteristic Theory Applied to Transonic Flows”, *14<sup>th</sup> International Conference on Numerical Methods in Fluid Dynamics*, 2005.
- [59] Pointwise, Grid Generation Software, ver. 18.2
- [60] Çengel Y., Cimbala J. M., “Fluid Mechanics Fundamentals and Applications”, McGraw-Hill Higher Education, 2006.
- [61] Minitab, Statistical Calculations Computer Software, ver. 2018
- [62] Whitcomb P. J., Larntz K., “The Role of Pure Error on Normal Probability Plots”, StatEase Publication.
- [63] Minitab, “Minitab 18 Support : Methods and Formulas for the Effects Plots in Analyze Factorial Design”, <https://support.minitab.com/en-us/minitab/18/help-and-how-to/modeling-statistics/doe/how-to/factorial/analyze-factorial-design/methods-and-formulas/effects-plots/> Last accessed 31.01.2021.
- [64] Lenth R. V., “Lenth’s Method for Analysis of Unreplicated Experiments”, *Encyclopedia of Statistics in Quality, and Reliability*, John Wiley & Sons, 2014.
- [65] Antony J., “Design of Experiments for Engineers and Scientists”, Elsevier, 2003.
- [66] Abbot I. H., Doenhoff A. E. V., “Theory of Wing Sections Including a Summary of Airfoil Data”, Dover Publications, 1960.
- [67] Riegels F. W., “Aerofoil Sections Results From Wind-Tunnel Investigations Theoretical Foundations”, London Butterworths, pp. 5-14, 1961.

- [68] Hale F. J., "Introduction to Aircraft Performance, Selection and Design", John Wiley, 1984.
- [69] Grabcad Embraer 312 Tucano CAD file, [www.grabcad.com/library/emb-312-tucano-t-27-smoke-squadron-1](http://www.grabcad.com/library/emb-312-tucano-t-27-smoke-squadron-1). Last accessed: 06.02.2021



## APPENDICES

### A. Additional Design Points for Main Factors

Additional Design Point	Wing Span (m)	Root Chord Length (m)	Tip Chord Lengt h (m)	Dihedral Angle (deg)	Quarter Chord Sweep Angle (deg)	Tip Twist Angle (deg)
1	9.01	1.85	0.86	0	0	0
2	10.63	1.85	0.86	0	0	0
3	7.38	2.09	0.86	0	0	0
4	7.38	1.03	0.86	0	0	0
5	7.38	1.85	1.03	0	0	0
6	7.38	1.85	1.20	0	0	0
7	7.38	1.85	0.86	3.33	0	0
8	7.38	1.85	0.86	6.66	0	0
9	7.38	1.85	0.86	0	3.33	0
10	7.38	1.85	0.86	0	6.66	0
11	7.38	1.85	0.86	0	0	-1
12	7.38	1.85	0.86	0	0	-2

**B. Additional Design Points for Wingspan – Root Chord Length Interaction**

<b>Additional Design Point</b>	<b>Wing Span (m)</b>	<b>Root Chord Length (m)</b>	<b>Tip Chord Length (m)</b>	<b>Dihedral Angle (deg)</b>	<b>Quarter Chord Sweep Angle (deg)</b>	<b>Tip Twist Angle (deg)</b>
13	12.26	2.09	0.86	0	0	0
14	9.01	2.09	0.86	0	0	0
15	10.63	2.09	0.86	0	0	0
16	12.26	2.33	0.86	0	0	0
17	9.01	2.33	0.86	0	0	0
18	10.63	2.33	0.86	0	0	0
19	9.01	2.57	0.86	0	0	0
20	10.63	2.57	0.86	0	0	0

**C. Additional Design Points for Tip Chord Length – Root Chord Length Interaction**

<b>Additional Design Point</b>	<b>Wing Span (m)</b>	<b>Root Chord Length (m)</b>	<b>Tip Chord Length (m)</b>	<b>Dihedral Angle (deg)</b>	<b>Quarter Chord Sweep Angle (deg)</b>	<b>Tip Twist Angle (deg)</b>
21	7.38	2.09	1.03	0	0	0
22	7.38	2.09	1.20	0	0	0
23	7.38	2.09	1.37	0	0	0
24	7.38	2.33	1.03	0	0	0
25	7.38	2.33	1.20	0	0	0
26	7.38	2.33	1.37	0	0	0
27	7.38	2.57	1.03	0	0	0
28	7.38	2.57	1.20	0	0	0

**D. Additional Design Points for Wingspan – Dihedral Angle Interaction**

<b>Additional Design Point</b>	<b>Wing Span (m)</b>	<b>Root Chord Length (m)</b>	<b>Tip Chord Length (m)</b>	<b>Dihedral Angle (deg)</b>	<b>Quarter Chord Sweep Angle (deg)</b>	<b>Tip Twist Angle (deg)</b>
29	9.01	1.85	0.86	3.33	0	0
30	9.01	1.85	0.86	6.66	0	0
31	9.01	1.85	0.86	10.00	0	0
32	10.63	1.85	0.86	3.33	0	0
33	10.63	1.85	0.86	6.66	0	0
34	10.63	1.85	0.86	10.00	0	0
35	12.26	1.85	0.86	3.33	0	0
36	12.26	1.85	0.86	6.66	0	0

**E. Additional Design Points for Root Chord Length – Dihedral Angle Interaction**

<b>Additional Design Point</b>	<b>Wing Span (m)</b>	<b>Root Chord Length (m)</b>	<b>Tip Chord Length (m)</b>	<b>Dihedral Angle (deg)</b>	<b>Quarter Chord Sweep Angle (deg)</b>	<b>Tip Twist Angle (deg)</b>
37	7.38	2.09	0.86	3.33	0	0
38	7.38	2.09	0.86	6.66	0	0
39	7.38	2.09	0.86	10.00	0	0
40	7.38	2.33	0.86	3.33	0	0
41	7.38	2.33	0.86	6.66	0	0
42	7.38	2.33	0.86	10.00	0	0
43	7.38	2.57	0.86	3.33	0	0
44	7.38	2.57	0.86	6.66	0	0